Sensitivity of cloud phase distribution to cloud microphysics and thermodynamics in simulated deep convective clouds and SEVIRI retrievals

Cunbo Han[1,2], Corinna Hoose[1], Martin Stengel[3], Quentin Coopman[4], Andrew Barrett[1]

1. Institute of Meteorology and Climate Research (IMK-TRO), Karlsruhe Institute of Technology, Karlsruhe, Germany
2. State Key Laboratory of Tibetan Plateau Earth System, Environment and Resources (TPESER), Institute of Tibetan Plateau Research, Chinese Academy of Sciences, Beijing, China
3. Deutscher Wetterdienst (DWD), Offenbach, Germany
4. Department of Atmospheric and Oceanic Sciences, McGill University, Montreal, Canada

Correspondence to: Cunbo Han (cunbo.han@hotmail.com) and Corinna Hoose (corinna.hoose@kit.edu)

Abstract:

The formation of ice in clouds is an important process in mixed-phase clouds, and the radiative properties and dynamical developments of clouds strongly depend on their partitioning between liquid and ice phases. In this study, we investigate the sensitivities of the cloud phase to ice-nucleating particle (INP) concentration and thermodynamics. Experiments are conducted using the ICOsahedral Nonhydrostatic model (ICON) at the convection-permitting resolution of about 1.2 km on a domain covering significant parts of central Europe, and are compared to two different retrieval products based on SEVIRI measurements. We select a day with multiple isolated deep convective clouds, reaching a homogeneous freezing temperature at the cloud top. The simulated cloud liquid pixel fractions are found to decrease with increasing INP concentration both within clouds and at the cloud top. The decrease in cloud liquid pixel fraction is not monotonic but is stronger in high INP cases. Cloud-top glaciation temperatures shift toward warmer temperatures with increasing INP concentration by as much as 8 °C. Moreover, the impact of INP concentration on cloud phase partitioning is more pronounced at the cloud top than within the cloud. Moreover, initial and lateral boundary temperature fields are perturbed with increasing and decreasing temperature increments from 0 to +/-3K and +/-5K between 3 and 12 km. Perturbing the initial thermodynamic state is also found to affect the cloud phase distribution systematically. However, the simulated cloud-top liquid pixel fraction, diagnosed using radiative transfer simulations as input to a satellite forward operator and two different satellite remote sensing retrieval algorithms, deviates from one of the satellite products regardless of perturbations in the INP concentration or the initial thermodynamic state for warmer sub-zero temperatures, while agreeing with the other retrieval scheme much better, in particular for the high INP and high convective available potential energy (CAPE) scenarios. Perturbing the initial thermodynamic state, which artificially increases the instability of the mid- and upper-troposphere, brings the simulated cloud-top liquid pixel fraction closer to the satellite observations, especially in the warmer mixed-phase temperature range.

Keywords: Mixed-phase clouds, deep convection, INP, thermodynamics, satellite forward operator, remote-sensing retrieval algorithms

Key points:

1. Cloud properties are retrieved using a satellite forward operator and remote sensing retrieval algorithms with ICON simulations as input. To our knowledge, it is the first time this approach has been used to retrieve cloud phase and other microphysical variables.

2. Glaciation temperature shifts towards a warmer temperature with increasing INP concentration both within the cloud and at the cloud top. Initial thermodynamic states affect the cloud phase distribution significantly as well.

3. Simulated cloud-top liquid pixel fraction matches the satellite observations in the high INP and high CAPE scenarios.

1. Introduction

In the temperature range between 0 and -38°C, ice particles and supercooled liquid droplets can coexist in mixed-phase clouds. Mixed-phase clouds are ubiquitous in Earth's atmosphere, occurring at all latitudes from the poles to the tropics. Because of their widespread nature, mixed-phase processes play a critical role in the life cycle of clouds, precipitation formation, cloud electrification, and the radiative energy balance on both regional and global scales (Korolev et al., 2017). Deep convective clouds are always mixed-phase clouds, and their cloud tops reach the homogeneous freezing temperature, -38°C, in most cases. Despite the importance of mixed-phase clouds in shaping global weather and climate, microphysical processes for mixed-phase cloud formation and development are still poorly understood, especially ice formation processes. It is not surprising that the representation of mixed-phase clouds is one of the big challenges in weather and climate models (McCoy et al., 2016; Korolev et al., 2017; Hoose et al., 2018; Takeishi and Storelvmo, 2018; Vignon et al., 2021; Zhao et al., 2021).

The distribution of cloud phase has been found to impact cloud thermodynamics and Earth's radiation budget significantly (Korolev et al., 2017; Matus and L'Ecuyer, 2017; Hawker et al., 2021). The freezing of liquid droplets releases latent heat and hence affects the thermodynamic state of clouds. Moreover, distinct optical properties of liquid droplets and ice particles exert different impacts on cloud's shortwave and longwave radiation. Simulation and observation studies reported that the cloud phase in the mixed-phase temperature range of convective clouds is influenced by aerosol and plays a significant role in the development into deeper convective systems (Li et al., 2013; Sheffield et al., 2015; Mecikalski et al., 2016). Observational studies reveal that the cloud phase distribution is highly temperature-dependent and influenced by multiple factors, for example, cloud type and cloud microphysics (Rosenfeld et al., 2011; Coopman et al., 2020). Analyzing passive satellite observations of mixed-phase clouds over the Southern Ocean, Coopman et al. (2021) found that cloud ice fraction increases with increasing cloud effective radius. Analysis of both passive and active satellite datasets reveals an increase in supercooled liquid fraction with cloud optical thickness (Bruno et al., 2021).

101 A number of in-situ observations of mixed-phase clouds have been made in the past
102 several decades, covering stratiform clouds (Pinto, 1998; Korolev and Isaac, 2006;
103 Noh et al., 2013) and convective clouds (Rosenfeld and Woodley, 2000; Stith et al.,
104 2004; Taylor et al., 2016). Aircraft-based observations of mixed-phase clouds
105 properties reveal that the frequency distribution of the ice water fraction has a U-
106 shape with two explicit maxima, one for ice water fraction smaller than 0.1 and the
107 other for ice water fraction larger than 0.9, and the frequency of occurrence of mixed-
108 phase clouds is approximately constant when the ice water fraction is in the range
109 between 0.2 and 0.5 (Korolev et al., 2003; Field et al., 2004; Korolev et al., 2017).
110 These findings are very useful constraints of numerical models (Lohmann and
111 Hoose, 2009; Grabowski et al., 2019). However, in-situ observations of mixed-phase
112 cloud microphysics are technically difficult and sparse in terms of spatial and
113 temporal coverage. Thus, understanding ice formation processes and determining
114 the climatological significance of mixed-phase clouds have proved difficult using
115 existing in-situ observations only.
116
117 Both observations and simulations reveal that ice-nucleating particles (INPs) impact
118 deep convective cloud properties including the persistence of deep convective
119 clouds and precipitation (Twohy, 2015; Fan et al., 2016). However, the impact of
120 INPs on precipitation from deep convective clouds is still uncertain and may depend
121 on precipitation and cloud types (van den Heever et al., 2006; Min et al., 2009; Fan
122 et al., 2010; Li and Min, 2010). Although the effects of INPs on convective
123 precipitation are not conclusive, it is certain that the interactions between convective
124 clouds and INPs affect cloud microphysical properties and hence cloud phase
125 distributions. In addition, previous numerical modeling studies on cloud-aerosols
126 interactions have focused on influences of aerosols acting as cloud condensation
127 nuclei (CCN) (Fan et al., 2016), which are linked to the ice phase e.g. through
128 impacts on the riming efficiency (Barrett and Hoose, 2023). Given the limited
129 knowledge on ice formation in deep convective clouds and significant uncertainties in
130 ice nucleation parameterizations, it is necessary to conduct sensitivity simulations to
131 investigate how ice formation processes are influenced by INP concentrations and
132 thermodynamic states in deep convective clouds.
133

134 In this study, with the help of realistic convection-permitting simulations using two-
135 moment microphysics, we address how and to what extent INP concentration and
136 thermodynamic state affect the in-cloud and cloud-top phase distributions in deep
137 convective clouds. In particular, cloud properties are retrieved using a satellite
138 forward operator and remote sensing retrieval algorithms with radiative transfer
139 simulations as input for a fair comparison to observations from SEVIRI. This method
140 allows us to compare model simulated cloud properties with remote sensing cloud
141 products directly, and is, to our knowledge, the first time this approach is used for the
142 cloud phase and related microphysical variables. We aim to evaluate the satellite
143 retrieval algorithms and investigate whether passive satellite cloud products can
144 detect cloud microphysical and thermodynamical perturbations.
145
146 This paper is structured as follows: In section 2, we introduce our model setups and
147 the experiment design, the satellite forward operator, remote sensing retrieval
148 algorithms, and datasets. Simulation results for the sensitivity experiments are
149 shown in section 3. Section 4 presents discussions; and we summarize the study
150 and draw conclusions in section 5.

151 **2. Data and Method**

152 **2.1. Model description**

153 The Icosahedral Nonhydrostatic (ICON) model (Zängl et al., 2015) is a state-of-the-
154 art unified modeling system offering three physics packages, which are dedicated to
155 numerical weather prediction (NWP), climate simulation, and large-eddy simulation.
156 ICON is a fully compressible model and has been developed collaboratively between
157 the German Weather Service (DWD), Max Planck Institute for Meteorology, German
158 Climate Computing Center (DKRZ), and Karlsruhe Institute of Technology (KIT). In
159 order to maximize the model performance and to remove the singularity at the poles,
160 ICON solves the prognostic variables suggested by Gassmann and Herzog (2008),
161 on an unstructured triangular grid with C-type staggering based on a successive
162 refinement of a spherical icosahedron (Wan et al., 2013). Governing equations are
163 described in Wan et al. (2013) and Zängl et al. (2015). The DWD has operated the
164 ICON model at a spatial resolution of about 13 km on the global scale since January
165 2015. In the global ICON, the higher-resolution ICON-EU (resolution 7 km) nesting

166   area for Europe has been embedded since July 2015. In this study, ICON-2.6.4 with

167   the NWP physics package is used and initial and lateral boundary conditions are

168   provided by the ICON-EU analyses.

169

170   For cloud microphysics, we use an updated version of the two-moment cloud

171   microphysics scheme developed by Seifert and Beheng (2006). The two-moment

172   scheme predicts the number and mass mixing ratios of two liquid (cloud and rain)

173   and four solid (ice, graupel, snow, and hail) hydrometers. The cloud condensation

174   nuclei (CCN) activation is described following the parameterization developed by

175   Hande et al. (2016). Homogeneous freezing, including freezing of liquid water

176   droplets and liquid aerosols, is parametrized according to Kärcher et al. (2006).

177   Heterogeneous ice nucleation, including the immersion and deposition modes, is

178   parameterized as a function of temperature- and ice supersaturation-dependent INP

179   concentration (Hande et al., 2015). The INP concentration due to immersion

180   nucleation is described as the following equation:

181
$$C_{INP}(T_K) = A \times \exp[-B \times (T_K - T_{min})^C]$$
(1)

182   where T_k is the ambient temperature in Kelvin; A, B, and C are fitting constants with

183   different values to represent seasonally varying dust INP concentrations. The

184   parameterization for deposition INPs is simply scaled to the diagnosed relative

185   humidity with respect to ice (RH_{ice}):

186
$$C_{INP}(T_K, RH_{ice}) \approx C_{INP}(T_K) \times DSF(RH_{ice})$$
(2)

187
$$DSF(RH_{ice}) = a \times \arctan(b \times (RH_{ice} - 100) + c) + d$$
(3)

188   where $C_{INP}(T_K)$ is given by Equation (1); a, b, c, and d are constants. More details

189   are found in Hande et al. (2015).

190   **2.2. Simulation setup and sensitivity experiments**

191   In this study, the setup consists of two different domains with one-way nesting

192   covering a major part of central Europe (Figure 1). The horizontal resolution for the

193   nested domains is halved from 2400 m to 1200 m in the innermost domain, and the

194   time steps for the two domains are 12 s and 6 s, respectively. 150 vertical levels are

195   used, with a grid stretching towards the model top at 21 km. The vertical resolution is

196   the same for all horizontal resolutions and the lowest 1000 m encompass 20 layers.

197   A 1-D vertical turbulence diffusion and transfer scheme is used for the 2400 m and

198 1200 m resolutions, referred to as numerical weather prediction (NWP) physics.

199 Deep convection is assumed to be explicitly resolved, while shallow convection is

200 parameterized for both domains. The simulations are initialized at 00:00 UTC on the

201 study day from ICON-EU analyses and integrated for 24 hours. Simulation results

202 were saved every 15 minutes. At the lateral boundaries of the outer domain, the

203 simulation of the model is updated with 3-hourly ICON-EU analyses. The nested

204 domains are coupled online, and the outer domain provides lateral boundary

205 conditions to the inner domain.

206

207 In nature, INP concentration varies across multiple orders of magnitude (Hoose and

208 Möhler, 2012; Kanji et al., 2017). Thus, in our sensitivity experiments, heterogeneous

209 ice formation was scaled by multiplying the default INP concentration (Equation (1))

210 with a factor of 10^{-2}, 10^{-1}, 10^{1}, 10^{2}, 10^{3} for both immersion freezing and deposition ice

211 nucleation. Together with a case with default INP concentration (case CTRL) and

212 one case switching off the secondary-ice production via rime-splintering process (the

213 so called Hallet-Mossop process), 7 cases were created in total to investigate the

214 impact of primary and secondary ice formation on cloud phase distribution in deep

215 convective clouds.

216

217 In order to assess the sensitivity of the cloud phase to thermodynamics, initial and

218 lateral boundary temperature fields are modified with increasing and decreasing

219 temperature increments, named experiments INC and DEC, respectively. The

220 temperature increment is linearly increased/decreased with height from 0 K at 3 km

221 to +/-3K and +/-5K at 12 km, creating 4 sensitivity experiments DEC03, DEC05,

222 INC03, and INC05. Above 12 km, the increment is constant up to the model top.

223 Initial temperature profiles are shown in Figure 2. The increasing or decreasing

224 environmental temperature leads to changes in the lapse rate and the stability of the

225 atmosphere, and hence results in decrease or increase in the convective available

226 potential energy (CAPE), respectively (Barthlott and Hoose, 2018). Thus, the CAPE

227 increases monotonically from case INC05 (spatial-averaged CAPE at 9:00 UTC: 413

228 J kg^{-1}) to case CTRL (724 J kg^{-1}) and finally to DEC05 (1235 J kg^{-1}). Note that the

229 relative humidity increases/decreases with decreasing/increasing temperature as the

230 specific humidity is unperturbed. The perturbations of INP concentration and

231 initial/lateral temperature profiles are motivated by Hoose et al. (2018) and Barthlott

and Hoose (2018), respectively. Complementary to these earlier studies, we now investigate an ensemble of several deep convective clouds and focus on influences of INP and thermodynamics on cloud phase distribution. Short descriptions of all sensitivity experiments performed in this study are listed in Table 1.

2.3. Satellite observations and retrieval algorithms

The Spinning Enhanced Visible and Infrared Imager (SEVIRI) is a 12-channel imager on board the geostationary Meteosat Second Generation (MSG) satellites. SEVIRI has one high spatial resolution visible channel (HRV) and 11 spectral channels from 0.6 to 14 μm with a 15 min revisit cycle and a spatial resolution of 3 km at nadir (Schmetz et al., 2002). Based on the spectral measurements of SEVIRI, a cloud property data record, the CLAAS-2 dataset (CLoud property dAtAset using SEVIRI, Edition 2), has been generated in the framework of the EUMETSAT Satellite Application Facility on Climate Monitoring (CM SAF) (Benas et al., 2017). CLAAS-2 is the successor of CLAAS-1 (Stengel et al., 2014), for which retrieval updates have been implemented in the algorithm for the detection of clouds compared to CLAAS-1 (Benas et al., 2017) with the temporal coverage being extended to 2004-2015. Retrieval algorithms for parameters that are important for this study are introduced below. Detailed descriptions for the retrieval algorithms are found in Stengel et al. (2014) and Benas et al. (2017) with the main features being summarized in the following.

The MSGv2012 software package is employed to detect clouds and their vertical placement (Derrien and Le Gléau, 2005; Benas et al., 2017). Multi-spectral threshold tests, which depend on illumination and surface types, among other factors, are performed to detect cloud appearances. Each satellite pixel is assigned to categories of cloud-filled, cloud-free, cloud water contaminated, or snow/ice contaminated. Cloud top pressure (CTP) is retrieved with different approaches using input from SEVIRI channels at 6.2, 7.3, 10.8, 12.0, and 13.4 μm (Menzel et al., 1983; Schmetz et al., 1993; Stengel et al., 2014; Benas et al., 2017). Cloud top height (CTH) and cloud top temperature (CTT) are derived from CTP using ancillary data for temperature and humidity profiles from ERA-Interim (Dee et al., 2011). The cloud top phase (CPH) retrieval is based on a revised version of the multispectral algorithm

264 developed by Pavolonis et al. (2005). Clouds are categorized initially into six types,

265 that are liquid, supercooled, opaque ice, cirrus, overlap, and overshooting.

266 Subsequently, the binary cloud phase (liquid or ice) is generated based on the six

267 categories (Benas et al., 2017). Cloud optical and microphysical properties are

268 retrieved using the Cloud Physical Properties (CPP) algorithm (Roebeling et al.,

269 2006). SEVIRI visible (0.6 µm) and near-infrared (1.6 µm) measurements are used

270 to calculate cloud optical thickness (COT) and cloud particle effective radius (r_e) by

271 applying the Nakajima and King (1990) approach in the CPP algorithm (Stengel et

272 al., 2014; Benas et al., 2017). Liquid water path (LWP) and ice water path (IWP) are

273 then computed as a function of liquid/ice water density, COT, and r_e of cloud water

274 and cloud ice following the scheme developed by Stephens (1978).

275

276 In this study we used instantaneous CLAAS-2 data with temporal resolution of 15

277 minutes and on native SEVIRI projection and resolution. In addition to the CLAAS-2

278 dataset, the recently developed software suite SEVIRI_ML (Philipp and Stengel

279 (2023) in preparation; code available on Github:

280 https://github.com/danielphilipp/seviri_ml) was applied to the SEVIRI measurements

281 to obtain cloud top phase and cloud top temperature for the selected case.

282 SEVIRI_ML uses a machine learning approach calibrated against Cloud-Aerosol

283 Lidar with Orthogonal Polarization (CALIOP) data. One feature of the SEVIRI_ML is

284 that it also provides pixel-based uncertainties such that values with low reliability can

285 be filtered out. We applied the retrieval algorithms to the model simulations in this

286 study and compared the results to satellite observations. A similar strategy was used

287 by Kay et al. (2018) for the evaluation of precipitation in a climate model with

288 CloudSat observations and termed "scale-aware and definition-aware evaluation".

289 **2.4. Satellite forward operators**

290 In order to compare simulation results and satellite observations directly, SEVIRI-like

291 spectral reflectance and brightness temperatures are calculated using the radiative

292 transfer model for TOVS (RTTOV, v12.3)(Saunders et al., 2018). RTTOV is a fast

293 radiative transfer model for simulating top-of-atmosphere radiances from passive

294 visible, infrared, and microwave downward-viewing satellite radiometers. It has been

295 widely used in simulating synthetic satellite images and assimilating radiances in

296 numerical models ([Saunders et al., 2018](); [Pscheidt et al., 2019](); [Senf et al., 2020]();

297 [Geiss et al., 2021](); [Rybka et al., 2021]()).

298

299 In this work, ICON simulated surface skin temperature, near-surface pressure,

300 temperature, specific humidity, wind velocity, total liquid water content, total ice water

301 content, and effective radius of cloud liquid and cloud ice are used as input to drive

302 the RTTOV model. Before inputting to the RTTOV model, ICON simulations are

303 remapped onto SEVIRI's full disc coordinate. Brightness temperatures from 8

304 channels (at 3.9, 6.2, 7.3, 8.7, 9.7, 10.8, 12.0, and 13.4 μm) and reflectance from 3

305 channels (at 0.6, 0.8, and 1.6 μm) simulated by the RTTOV model are used as input

306 to run the remote sensing retrieval algorithms to derive CLAAS-2-like and

307 SEVIRI_ML-like retrievals, named ICON_RTTOV_CLAAS-2 and

308 ICON_RTTOV_SEVIRI_ML products, respectively.

309 **2.5. Synoptic overview**

310 The day 06 June 2016 was selected to analyze, which was dominated by

311 summertime deep convection located in central Europe. The synoptic forcing was

312 weak on the day, and convection was triggered mainly by local thermal instabilities.

313 The day has been discussed frequently in previous studies in terms of convection

314 triggering, cloud microphysics, and its parameterizations ([Keil et al., 2019](); [Geiss et](

315 [al., 2021]()).

316 **3. Results and discussion**

317 Perturbing INP concentration and temperature profiles directly affects microphysical

318 and thermodynamic processes of the developing deep convective clouds, and hence

319 impact in-cloud and cloud-top phase distributions. The following section shows

320 results and discussions on the sensitivities of cloud phase and cloud microphysics to

321 INP concentration and thermodynamic perturbations.

322 **3.1. Spatial distribution of cloud properties**

323 Before analyzing the results of sensitivity experiments, retrieved cloud properties via

324 RTTOV and the CLAAS-2 retrieval scheme for the CTRL case are compared to

325 CLAAS-2 products. Spatial distributions of derived LWP, IWP, and COT at 13:00

326 UTC of the CTRL case and CLAAS-2 satellite observation are shown in Figure *3*.

327 Discrepancies are found between ICON simulation and CLAAS-2 satellite

328 observations in terms of spatial coverage and intensity. The ICON simulation

329 overestimates the cloud coverage of low-level liquid clouds compared to CLAAS-2

330 satellite observations, while LWP derived from the ICON simulation (case CTRL) is

331 smaller and more homogeneously distributed than that from the CLAAS-2

332 observation (Figure 3a and 3b). The spatial distributions of IWP and COT represent

333 the approximate location and spatial extension of deep convective clouds in this

334 study. The ICON simulation could reproduce cores of deep convective clouds of a

335 number and spacing comparable to observations, while the spatial extension and

336 intensity of individual deep convective clouds are not simulated very well by the

337 ICON model. The ICON simulation underestimates the spatial extension of deep

338 convective clouds but overestimates IWP and COT outside the convective cores

339 compared to the CLAAS-2 observation (Figure *3*c-f).

340

341 Overall, the simulated clouds appear to be too homogeneous without sufficient

342 internal structure. Geiss et al. (2021) also reported significant deviations between

343 model simulations and satellite observations. The error sources are manifold and

344 may originate from the model physics as well as from the forward operator and the

345 retrieval algorithm. Geiss et al. (2021) investigated the sensitivity of derived visible

346 and infrared observation equivalents to model physics and operator settings. They

347 found that the uncertainty of the visible forward operator is sufficiently low while

348 infrared channels could bring errors in cloud-top variables. Geiss et al. (2021)

349 concluded that the primary source of deviations is mainly from model physics,

350 especially model assumptions on subgrid-scale clouds. In addition to the subgrid-

351 scale cloud scheme, multiple critical cloud microphysical processes missing from the

352 model, introducing significant uncertainties into the simulation results. For example,

353 entrainment mixing process is not resolved or parameterized in the model, which has

354 essential influences on processes at cloud boundaries and hence the cloud

355 properties (Mellado, 2017). Moreover, secondary ice processes including droplet

356 shattering and collisional breakup due to ice particles collisions are missing, which

357 have significant impacts on the cloud ice microphysics (Sullivan et al., 2018;

358 Sotiropoulou et al., 2021).

3.2. Sensitivity of microphysical properties to INP perturbation

Perturbing INP concentration results in a direct influence on the heterogeneous freezing processes and hence impacts on cloud microphysical properties. Systematic variations have been found in the spatial- and time-averaged profiles of mass mixing ratios of cloud hydrometeors as shown in Figure 4. All profiles discussed here are averaged over cloudy pixels (defined as having a condensed mass of cloud water plus total cloud ice greater than a threshold of 1.0×10^{-5} kg kg^{-1}) and over the time period from 9:00 to 19:00 UTC, when convection was well developed. The mass concentration of ice crystals decreases with increasing INP concentration (Figure 4a). However, the mass concentration of snow, graupel, and rainwater increase with increasing INP concentration, especially in the high INP concentration cases (cases A$\times 10^2$ and A$\times 10^3$).

In order to further reveal why ice crystal mass concentration decreases with increasing INP concentration, we investigate process rates related to ice particle nucleation and growth. Figure 5 shows spatial- and time-averaged (from 9:00 to 19:00 UTC) profiles of process rates for homogeneous freezing, heterogeneous freezing, secondary ice production via the rime-splintering process, cloud droplets rimed with ice crystals, rain droplets rimed with ice crystals, and collection between ice and ice crystals. Heterogeneous freezing (Figure 5a) includes processes of immersion freezing, deposition ice nucleation, and immersion freezing of liquid aerosols (Kärcher et al., 2006; Hande et al., 2015), see also equations (1) and (2). Process rates of heterogeneous freezing increase significantly with increasing INP concentration compared to the CTRL (Figure 5a). Compensating the change in heterogeneous freezing, process rates of homogeneous freezing decrease significantly with increasing INP concentration (Figure 5b). However, a decrease in INP concentration (compared to the CTRL) does not have a strong influence on the heterogeneous freezing mass rate, which is already low compared to the other processes in CTRL. Riming processes of cloud droplets and rain droplets onto ice crystals are greatly invigorated due to enhanced INP concentration (Figure *5*d and 5e). Moreover, process rates of secondary ice production due to rime-splintering are strengthened as well due to the increase in rimed ice, albeit much lower values. Figure *5*f shows process rates of collection between ice and ice crystals. Process

392 rates of collection between ice and ice particles increase with increasing INP

393 concentration, especially in high INP concentration cases (cases A$\times$10^2 and A$\times$10^3).

394 Process rates of collection of other ice particles all increase with increasing INP

395 concentration, similar to the collection between ice and ice crystals (not shown). The

396 increase in the riming of clouds and rain droplets onto ice crystals and collections

397 between ice particles leads to the increase in the mass concentration of snow,

398 graupel, and hail (Figure 4b and 4c). However, the total mass increase in snow,

399 graupel, and hail do not outbalance the decrease in the mass concentration of ice

400 crystals (Figure 4). The weakened homogeneous freezing is most likely the dominant

401 factor leading to the decrease in ice mass concentration in high INP cases,

402 considering the magnitude of the process rate of homogeneous freezing (Figure 5b).

403 Supercooled liquid and cloud droplets have been converted into ice crystals before

404 reaching the homogeneous freezing layer, leading to fewer supercooled droplets

405 remaining for homogeneous freezing. Even though homogeneous freezing is

406 weakened in high INP cases, the process rate of homogeneous freezing is still larger

407 than heterogeneous freezing, which means homogeneous freezing is the dominant

408 ice formation process in the convective clouds discussed in this study. Moreover, the

409 enhanced production of large ice particles (snow, graupel, and hail) in the highest

410 INP case, which sediment more rapidly to lower levels, leads to increased surface

411 precipitation by about 10% in the A$\times$10^3 case (not shown). Interestingly, ice crystal

412 effective radius (r_e^{ice}) increases monotonically with increasing INP concentration,

413 especially in the mixed-phase layer (Figure *4*e). Zhao et al. (2019) also reported an

414 increased r_e^{ice} with polluted continental aerosols in their simulated moderate

415 convection cases, and they attributed it to enhanced heterogeneous freezing and

416 prolonged ice crystal growth at higher INP loading.

417

418 This competition between homogeneous and heterogeneous freezing has been

419 discussed in previous studies (Heymsfield et al., 2005; Deng et al., 2018; Takeishi

420 and Storelvmo, 2018). In contrast, simulations of mixed-phase moderately deep

421 convective clouds by Miltenberger and Field (2021) indicate that cloud ice mass

422 concentration increases with increasing INP concentration, which is in opposition to

423 the findings in this work. The main reason is that the CTT is about -18°C in

424 Miltenberger and Field (2021)'s study, and heterogeneous freezing does not

425 compete with homogeneous freezing. Thus, results on INPs effects on glaciation
426 processes in convective clouds can be opposite under different conditions.

427 **3.3. Cloud liquid mass fraction**

428 Varying the INP concentration has a direct impact on the primary ice formation.
429 Thus, it affects cloud liquid mass fraction within the clouds (directly for all cloudy
430 layers where heterogeneous freezing is active and indirectly for warmer and colder
431 temperatures) and at the cloud top. Cloud liquid mass fraction is defined as the ratio
432 of mass mixing ratio between cloud droplets (q_c) and the sum of cloud droplets and
433 cloud ice crystals (q_i). In-cloud liquid mass fraction, sampled at a time interval of 15
434 minutes between 9:00 to 19:00 from all cloudy pixels, is shown as scatterplots
435 versus temperature in Figure 6a-d. The corresponding frequencies of the occurrence
436 of the temperature/liquid fraction bins are shown in Figure 6e-h. Similar analyses
437 were made by Hoose et al. (2018), but for idealized simulations of deep convective
438 clouds. In-cloud liquid mass fractions smaller than 0.5 are quite common already at
439 temperature just below -3 °C except for the case without rime-splintering process
440 ($A\times10^0$_NSIP). The decrease in INP concentrations has limited effects on the in-
441 cloud liquid mass fraction (Figure 6c and 6g), while a stronger influence has been
442 found in the case with enhanced INP concentration (Figure 6d and 6h). The number
443 of pixels having high liquid mass fraction values at temperatures lower than -30 °C
444 decreases with increasing INP concentration. In addition, more and more pixels
445 having liquid mass fraction smaller than 0.5 appear with increasing INP
446 concentration and the number of pure ice pixels increases with increasing INP
447 concentration as well. This is because higher INP concentration intensifies the
448 heterogeneous freezing processes (immersion freezing and deposition ice
449 nucleation) and invigorates the rime-splintering process as well (will be discussed in
450 section 3.4). Interestingly, at the lower end of the mixed-phase temperature range (-
451 38 ~ -28 °C), there are fewer pixels having high liquid mass fraction in the high INP
452 case, and those remaining are mainly the ones at high vertical velocities (above ~ 10
453 m/s). This is probably because supercooled droplets are more easily frozen in high
454 INP cases and stronger updrafts are needed to offset the Wegener-Begeron-
455 Findeisen process to maintain the supersaturation with respect to water. Switching
456 off the secondary ice production via rime-splintering process, pixels having a liquid

457   mass fraction smaller than 0.9 are reduced significantly at temperatures between -

458   10 °C and 0 °C (Figure 6b and 6f).

459

460   At the cloud top (Figure 7), the number of pixels having a liquid mass fraction smaller

461   than 0.5 increases with increasing INP concentration, which is the same as within

462   the clouds. "Cloud top" is defined as the height of the uppermost cloud layer (which

463   has a condensed mass of cloud water plus cloud total cloud ice greater than a

464   threshold of 1.0×10^{-5} kg kg^{-1}) in a pixel column. At the cloud top, the liquid mass

465   fraction has a more polarized distribution, with either large values or small values,

466   and intermediate values are less common than within the clouds. This is because the

467   vertical velocities at the cloud top are significantly smaller compared to that within

468   the cloud, which leads to a more efficient Wegener-Begeron-Findeisen process at

469   the cloud top.

470   **3.4. Liquid cloud pixel fraction**

471   Liquid cloud pixel fractions are calculated differently for model simulations and

472   retrieved cloud products. For simulation results, a cloudy pixel having a cloud liquid

473   mass fraction larger than 0.5 is counted as a liquid pixel, otherwise, it is an ice pixel.

474   Both CLAAS-2 and SEVIRI_ML products and the corresponding retrievals derived

475   from ICON simulations by the satellite forward operators (see section 2.4) provide

476   binary cloud phase information (liquid or ice) only. For these data, the liquid cloud

477   pixel fraction is calculated as the ratio between the number of liquid cloud pixels and

478   the sum of all cloudy pixels.

479

480   Liquid cloud pixel fractions within clouds and at the cloud top are shown in Figure 8.

481   Decrease in INP concentration has limited impacts on the liquid cloud pixel fraction

482   for in-cloud layers. Increase in INP concentration leads to a decrease in liquid cloud

483   pixel fraction but not monotonically (Figure 8a). The decrease in liquid cloud pixel

484   fraction is significant in the highest INP concentration case (case A$\times10^3$), while

485   decreases in intermediate INP concentration cases (cases A$\times10^1$ and A$\times10^2$) are

486   only obvious in temperature ranges from -30 °C to -20 °C and from -15 °C to -5 °C.

487   Moreover, liquid mass fraction decreases monotonically with increasing INP

488   concentration in the temperature range from about -15 to -35 ˚C both within the cloud

489   and at the cloud top (except for the lowest INP concentrations), and the decreasing

490   trend is more significant at the cloud top compared to within the cloud (not shown).

491   Switching off the rime-splintering process results in an increase in liquid cloud pixel

492   fraction in the temperature range between -10 °C and -3 °C, which is consistent with

493   the strong decrease in pixels of cloud liquid mass fraction lower than 0.9 in the same

494   temperature range (Figure 7b). The temperature at which the liquid cloud pixel

495   fraction equals 0.5 is often termed "glaciation temperature". The glaciation

496   temperature shifts slightly to a warmer temperature by ~2 °C at the highest INP

497   concentration case (case A$\times10^3$, Figure *8a*).

498

499   Sensitivities of the cloud phase to INP concentration are more complex at the cloud

500   top than inside the cloud. Liquid cloud pixel fractions at the cloud top calculated

501   directly from ICON simulations on its native grid (~1200 m) are shown in Figure 8b.

502   Cloud-top liquid pixel fraction decreases significantly with increasing INP

503   concentration. In the temperature range between -35 °C and -15 °C, where

504   heterogeneous freezing processes (immersion freezing and deposition nucleation)

505   are dominant, the impact of INP is most pronounced. Above -15 °C, the impact of

506   INP does not disappear, especially in the highest INP concentration case (case

507   A$\times10^3$). This is mostly likely due to the sedimentation of ice crystals from upper

508   layers and the secondary ice production invigorated by the Wegener-Begeron-

509   Findeisen process. Switching off the rime-splintering process increases cloud-top

510   liquid pixel fraction only slightly in the temperature range from -10 °C to -3 °C and is

511   almost identical to the control run (case CTRL) outside this temperature range.

512   Interestingly, the shift of glaciation temperature with increasing INP concentration is

513   about 8 °C (Figure 8b) at the cloud top, which is stronger than that inside the clouds

514   (~2 °C, Figure 8a). A possible explanation is that, typically, the vertical velocity at the

515   cloud top is smaller than within the cloud and the ice formation through the Wegener-

516   Bergeron-Findeisen process is expected to be more efficient. Thus, the Wegener-

517   Begeron-Findeisen process is more sensitive to INP perturbation at the cloud top

518   than within clouds, and leads to the glaciation temperature shifting to be more

519   significant at the cloud top.

520

17

521 Liquid cloud pixel fractions at the cloud top calculated directly from ICON simulations
522 on SEVIRI's grid (~ 5000 m) are shown in Figure 8c. They are noisier and do not
523 exhibit the small minimum between -10 °C and -3 °C related to rime-splintering, but
524 are otherwise very similar to Figure 8b. In contrast, the scale-aware and definition-
525 aware ICON_RTTOV_CLAAS-2 cloud-top liquid pixel fractions shown in Figure 8d
526 differ markedly from the direct or regridded model output. Above -23 °C, increase
527 and decrease in INP concentration both lead to a decrease in cloud-top liquid pixel
528 fraction at certain temperature, but the high INP concentration cases (cases $A \times 10^2$
529 and $A \times 10^3$), still exhibit the lowest liquid fractions, and case $A \times 10^0$_NSIP the highest.
530 Thus, the fingerprints of primary and secondary ice formation are retained in the
531 ICON_RTTOV_CLAAS-2 liquid fraction in this temperature range only for very strong
532 perturbations. At the same time, it must be noted that the decrease of the liquid pixel
533 fraction to values around 0.8 above -15 °C is not related to the rime-splintering
534 process, but to the application of the CLAAS-2 satellite simulator. Below -23 °C, in
535 the high INP cases $A \times 10^2$ and $A \times 10^3$, cloud-top liquid pixel fractions even increase
536 with increasing INP concentration. In moderate and low INP cases, the impacts of
537 INP perturbation are not pronounced. Moreover, the shape of cloud-top liquid pixel
538 fraction decreasing with cloud-top temperature is different from that in Figure 8b.
539 Here, the fingerprints of the ice formation processes are completely lost. As
540 demonstrated in Figure 8c, remapping of simulation data onto SEVIRI's coarser grid
541 is not the cause of liquid pixel fraction difference between direct ICON output and the
542 ICON_RTTOV_CLAAS-2 diagnostics, but the CLAAS-2 retrieval algorithm itself is
543 responsible.
544
545 The satellite observed cloud-top liquid pixel fraction from CLAAS-2 is plotted as a
546 grey dashed line in Figure 8d. It does not reach 1.0 for all cases even as the cloud-
547 top temperature is approaching 0 °C, and shows a different temperature dependency
548 than the simulated curves. No matter how strong the INP concentration and rime-
549 splintering are perturbed, the retrieved cloud-top liquid pixel fractions from simulation
550 data deviate strongly from the CLAAS-2 products. In this context one should note
551 that in particular cloud edges have been found to be problematic situations for the
552 cloud retrievals, being to some extent responsible for biasing the liquid-pixel fraction
553 towards smaller values, in particular for the CLAAS-2 data.

554

555 Finally, the comparison to observations is repeated with the SEVIRI_ML retrieval

556 scheme applied to both simulated radiances (ICON_RTTOV_SEVIRI_ML) and the

557 SEVIRI observations themselves (Figure 8e). As SEVIRI_ML provides uncertainty

558 estimates, pixels for which either the cloud mask uncertainty or the cloud phase

559 uncertainty is larger than 10% are filtered out. While this ensures that only very

560 certain values are kept, it has a significant impact on the number of remaining values

561 as more than 90% of the pixels are filtered out. The resulting liquid pixel fractions

562 ICON_RTTOV_SEVIRI_ML bear a much stronger similarity to the regridded model

563 output in Figure 8c. Remaining differences are a noisier behavior, a plateau of non-

564 zero liquid pixel fractions even below -40 °C, and a general shift to lower

565 temperatures. SEVIRI_ML applied to observations (dashed black line in Figure 8e),

566 with the same uncertainty criterion, exhibits the expected behavior with a liquid

567 fraction of approximately 1 above -10 °C and 0 below approximately -30 °C, and

568 results in a very good agreement to the A$\times10^3$ case. Generally, the SEVIRI_ML

569 retrieval algorithm is assumed to perform better than the CLAAS-2 scheme for both

570 cloud top temperature and cloud phase. This is because SEVIRI_ML employs state-

571 of-the-art neural networks to emulate CALIOP v4 data. Moreover, SEVIRI_ML

572 provides uncertainty estimates which facilitates fliting out pixels with high

573 uncertainties. Nevertheless, retrieval inaccuracies are unavoidable for passive

574 satellite retrievals which holds true for CLAAS-2 but also for SEVIRI_ML.

575 **3.5. Sensitivity of cloud phase to atmospheric stability perturbations**

576 In addition to the reference run (case CTRL), four cases with perturbations in initial

577 temperatures are analyzed. Mean updraft velocities increase gradually from the low

578 CAPE case INC05 to high CAPE case DEC05 (Figure 9) and cause differences in

579 cloud microphysics and cloud phase distributions.

580

581 In-cloud and cloud-top liquid cloud pixel fractions for the five cases are shown in

582 Figure 10. Systematic shifting of liquid cloud pixel fractions is detected both inside

583 clouds and at the cloud top. Liquid cloud pixel fraction decreases with increasing

584 CAPE from INC05 to DEC05. Both in-cloud and cloud-top glaciation temperatures

585 shift toward warmer temperatures as the CAPE increases from case INC05 to

586 DEC05. This is different from the results reported by [Hoose et al. (2018)](#) that cloud-
587 top glaciation temperatures hardly changed with increasing temperature in the
588 boundary-layer by 2 °C, and appears to be contradictory to the expectation that
589 stronger vertical velocities result in a lower glaciation temperature due to
590 suppression of the Wegener-Bergeron-Findeisen process ([Korolev, 2007](#)). Further
591 analysis (not shown) revealed that the mass concentration of cloud ice particle
592 increases while the mass concentration of cloud droplet decreases with the increase
593 in CAPE from case INC05 to DEC05. Moreover, homogeneous and heterogeneous
594 freezing are both enhanced in the high CAPE cases (Figure *11*), possibly due to
595 more transport of moisture to upper levels in the stronger updrafts (Figure *9*). With
596 more ice generated, the Wegener-Begeron-Findeisen process can be stimulated
597 despite the higher updrafts. Interestingly, cloud-top liquid pixel fractions from the two
598 high CAPE cases (cases DEC03 and DEC05) are closer to SEVIRI observations,
599 both using the CLAAS-2 retrieval (Figure 10c) and the SEVIRI_ML retrieval (Figure
600 10d), especially in the temperature range between -10 and -28 °C. Overall,
601 perturbing initial thermodynamic states or CAPE of convective clouds is as important
602 as and may even stronger than the modifications to cloud heterogeneous freezing
603 parameterizations.

604 **4. Conclusions**

605 Remote sensing products, which cover the entire globe, provide a unique opportunity
606 to constrain the representation of cloud microphysics in global and regional
607 numerical models. In this study, instead of comparing simulation results to satellite
608 observations directly, we derived cloud properties using a radiative transfer model
609 and two different satellite remote sensing retrieval algorithms and then performed the
610 comparison. This enables us to make apples-to-apples comparisons between model
611 simulations and satellite observations. A series of numerical experiments were
612 performed applying convection-permitting simulations with perturbations in INP
613 concentrations and initial thermodynamic states to investigate their impacts on cloud
614 phase distributions in deep convective clouds. Moreover, cloud properties were
615 derived using a satellite forward operator and retrieval algorithms with ICON
616 simulations as input, and compared with CLAAS-2 and SEVIRI_ML satellite cloud
617 products to evaluate whether satellite retrievals could detect perturbations in cloud

618 microphysics and thermodynamics. Uncertainties in the forward operator were
619 however not assessed in this study, which may influence the validity of
620 corresponding results in some extent.

621

622 INP concentration was found to have a significant role in shaping cloud phase
623 distributions both within clouds and at the cloud top. Cloud liquid pixel fraction
624 decreased with increasing INP concentration both within the cloud and at the cloud
625 top, indicating a higher glaciation temperature and more intense heterogeneous
626 freezing processes in enhanced INP concentration cases. Interestingly, the
627 influences of INP did not increase linearly but are more pronounced in the high INP
628 concentration cases. In addition, the shifting of glaciation temperature was more
629 significant at the cloud top than within the cloud, which means the impact of INP
630 concentration on cloud phase distribution is more pronounced at the cloud top. It
631 turned out that with the CLAAS-2 retrieval scheme, the INP sensitivity of the cloud-
632 top phase distribution was not detectable, while the SEVIRI_ML retrieval scheme, for
633 which the most uncertain pixels could be excluded, resulted in a better agreement
634 and retained the sensitivity to INP. In contrast, secondary ice production via rime-
635 splintering did not have a detectable impact on the cloud-top phase distribution.
636 Therefore, in future studies, we recommend using the SEVIRI_ML retrieval scheme
637 and SEVIRI_ML satellite-based cloud products.

638

639 Ice crystal mass concentration did not increase but decreases with increasing INP
640 concentrations in the simulated deep convective clouds. Process rate analyses
641 revealed that heterogeneous freezing process rates increased with increasing INP
642 concentration, while homogeneous freezing process rates decreased with increasing
643 INP concentration. The competition between heterogeneous freezing and
644 homogeneous freezing for water vapor suppressed ice formation via homogeneous
645 freezing, which was the dominant nucleation process in the simulated deep
646 convective clouds, and hence reduced the cloud ice mass concentration. The
647 increase in heterogeneous nucleation in high INP cases invigorated riming and
648 collection processes of ice particles, making it easier for small ice crystals to grow
649 into large ice aggregates and sediment to lower levels. This was the reason why
650 precipitation increases in enhanced INP cases.

651

652   Perturbations in initial thermodynamic states had a strong impact on the cloud phase

653   distribution both within the cloud and at the cloud top, although the used

654   perturbations might be rather large compared to initial condition uncertainty in a

655   weather forecasting context. Moreover, cloud thermodynamics can perturb the cloud

656   phase distribution even stronger than microphysics. To completely distinguish

657   microphysical impacts from thermodynamic impacts, applying a piggybacking

658   approach (Grabowski, 2015; Thomas et al., 2023) in future simulations is necessary.

659

660   Utilizing satellite forward operator (the RTTOV radiative model) and remote sensing

661   retrieval algorithms enabled us to derive cloud-top microphysical properties and

662   compare simulation results to satellite products more consistently. However, there

663   were significant differences in retrieved cloud-top liquid fractions between model

664   simulations and satellite products. The sources of errors were very complicated and

665   may come from simulation results, satellite operators, and retrieval algorithms, which

666   will be investigated in the future. Moreover, the cloud-top property analysis

667   presented in this study was based on domain-wide statistics, including clouds of

668   varying types. Statistical results could differ if individual clouds are tracked, as clouds

669   differ in different experiments in terms of locations and extensions. Although there

670   are significant uncertainties in satellite forward operators and retrieval algorithms,

671   passively remote-sensed cloud products provide potential opportunities to constrain

672   microphysical processes in numerical models.

673

674   Simulation results of this study revealed a close dependence of heterogeneous

675   freezing and cloud phase distribution on INP concentrations. Despite this finding, the

676   ice formation processes in deep convective clouds remain poorly understood. It is

677   necessary to investigate how and in which conditions the competition of

678   heterogeneous with homogeneous freezing for water vapor and cloud water depends

679   on INP availability and vertical velocities in different types of deep convective clouds.

680   Moreover, the importance of other secondary ice production processes than rime-

681   splintering (droplet shattering and collisional breakup) in deep convective clouds

682   need to be quantified in the future.

683

Competing interests

One of the (co-)authors (Corinna Hoose) is a member of the editorial board of Atmospheric Chemistry and Physics.

Acknowledgments

References

Barrett, A. I. and Hoose, C.: Microphysical pathways active within thunderstorms and their sensitivity to CCN concentration and wind shear, Journal of Geophysical Research: Atmospheres, 128, e2022JD036965, https://doi.org/10.1029/2022JD036965, 2023.

Barthlott, C. and Hoose, C.: Aerosol effects on clouds and precipitation over central Europe in different weather regimes, Journal of the Atmospheric Sciences, 75, 4247-4264, https://doi.org/10.1175/JAS-D-18-0110.1, 2018.

Benas, N., Finkensieper, S., Stengel, M., van Zadelhoff, G. J., Hanschmann, T., Hollmann, R., and Meirink, J. F.: The MSG-SEVIRI-based cloud property data record CLAAS-2, Earth Syst. Sci. Data, 9, 415-434, http://dx.doi.org/10.5194/essd-9-415-2017, 2017.

Bruno, O., Hoose, C., Storelvmo, T., Coopman, Q., and Stengel, M.: Exploring the cloud top phase partitioning in different cloud types using active and passive satellite sensors, Geophysical Research Letters, 48, e2020GL089863-e082020GL089863, https://doi.org/10.1029/2020GL089863, 2021.

Coopman, Q., Hoose, C., and Stengel, M.: Analysis of the thermodynamic phase transition of tracked convective clouds based on geostationary satellite observations, Journal of Geophysical Research: Atmospheres, 125, e2019JD032146, https://doi.org/10.1029/2019JD032146, 2020.

Coopman, Q., Hoose, C., and Stengel, M.: Analyzing the thermodynamic phase partitioning of mixed phase clouds over the southern ocean using passive satellite observations, Geophysical Research Letters, 48, e2021GL093225, https://doi.org/10.1029/2021GL093225, 2021.

Dee, D. P., Uppala, S. M., Simmons, A. J., Berrisford, P., Poli, P., Kobayashi, S., Andrae, U., Balmaseda, M. A., Balsamo, G., Bauer, P., Bechtold, P., Beljaars,

A. C. M., van de Berg, L., Bidlot, J., Bormann, N., Delsol, C., Dragani, R., Fuentes, M., Geer, A. J., Haimberger, L., Healy, S. B., Hersbach, H., Hólm, E. V., Isaksen, L., Kållberg, P., Köhler, M., Matricardi, M., McNally, A. P., Monge-Sanz, B. M., Morcrette, J. J., Park, B. K., Peubey, C., de Rosnay, P., Tavolato, C., Thépaut, J. N., and Vitart, F.: The ERA-Interim reanalysis: configuration and performance of the data assimilation system, Quarterly Journal of the Royal Meteorological Society, 137, 553-597, https://doi.org/10.1002/qj.828, 2011.

Deng, X., Xue, H., and Meng, Z.: The effect of ice nuclei on a deep convective cloud in South China, Atmospheric Research, 206, 1-12, https://doi.org/10.1016/j.atmosres.2018.02.013, 2018.

Derrien, M. and Le Gléau, H.: MSG/SEVIRI cloud mask and type from SAFNWC, International Journal of Remote Sensing, 26, 4707-4732, https://doi.org/10.1080/01431160500166128, 2005.

Fan, J., Comstock, J. M., and Ovchinnikov, M.: The cloud condensation nuclei and ice nuclei effects on tropical anvil characteristics and water vapor of the tropical tropopause layer, Environmental Research Letters, 5, 044005, https://doi.org/10.1088/1748-9326/5/4/044005, 2010.

Fan, J., Wang, Y., Rosenfeld, D., and Liu, X.: Review of aerosol–cloud interactions: Mechanisms, significance, and challenges, Journal of the Atmospheric Sciences, 73, 4221-4252, https://doi.org/10.1175/JAS-D-16-0037.1, 2016.

Field, P. R., Hogan, R. J., Brown, P. R. A., Illingworth, A. J., Choularton, T. W., Kaye, P. H., Hirst, E., and Greenaway, R.: Simultaneous radar and aircraft observations of mixed-phase cloud at the 100 m scale, Quarterly Journal of the Royal Meteorological Society, 130, 1877-1904, https://doi.org/10.1256/qj.03.102, 2004.

Gassmann, A. and Herzog, H.-J.: Towards a consistent numerical compressible non-hydrostatic model using generalized Hamiltonian tools, Quarterly Journal of the Royal Meteorological Society, 134, 1597-1613, http://dx.doi.org/10.1002/qj.297, 2008.

Geiss, S., Scheck, L., de Lozar, A., and Weissmann, M.: Understanding the model representation of clouds based on visible and infrared satellite observations, Atmos. Chem. Phys., 21, 12273-12290, https://doi.org/10.5194/acp-21-12273-2021, 2021.

Grabowski, W. W.: Untangling microphysical impacts on deep convection applying a novel modeling methodology, Journal of the Atmospheric Sciences, 72, 2446-2464, https://doi.org/10.1175/JAS-D-14-0307.1, 2015.

Grabowski, W. W., Morrison, H., Shima, S.-I., Abade, G. C., Dziekan, P., and Pawlowska, H.: Modeling of cloud microphysics: Can we do better?, Bulletin of the American Meteorological Society, 100, 655-672, https://doi.org/10.1175/BAMS-D-18-0005.1, 2019.

Hande, L. B., Engler, C., Hoose, C., and Tegen, I.: Seasonal variability of Saharan desert dust and ice nucleating particles over Europe, Atmos. Chem. Phys., 15, 4389-4397, http://dx.doi.org/10.5194/acp-15-4389-2015, 2015.

Hande, L. B., Engler, C., Hoose, C., and Tegen, I.: Parameterizing cloud condensation nuclei concentrations during HOPE, Atmos. Chem. Phys., 16, 12059-12079, http://dx.doi.org/10.5194/acp-16-12059-2016, 2016.

Hawker, R. E., Miltenberger, A. K., Wilkinson, J. M., Hill, A. A., Shipway, B. J., Cui, Z., Cotton, R. J., Carslaw, K. S., Field, P. R., and Murray, B. J.: The temperature dependence of ice-nucleating particle concentrations affects the

24

radiative properties of tropical convective cloud systems, Atmos. Chem. Phys., 21, 5439-5461, https://doi.org/10.5194/acp-21-5439-2021, 2021.

Heymsfield, A. J., Miloshevich, L. M., Schmitt, C., Bansemer, A., Twohy, C., Poellot, M. R., Fridlind, A., and Gerber, H.: Homogeneous ice nucleation in subtropical and tropical convection and its influence on cirrus anvil microphysics, Journal of the Atmospheric Sciences, 62, 41-64, http://dx.doi.org/10.1175/JAS-3360.1, 2005.

Hoose, C. and Möhler, O.: Heterogeneous ice nucleation on atmospheric aerosols: a review of results from laboratory experiments, Atmos. Chem. Phys., 12, 9817-9854, https://doi.org/10.5194/acp-12-9817-2012, 2012.

Hoose, C., Karrer, M., and Barthlott, C.: Cloud top phase distributions of simulated deep convective clouds, Journal of Geophysical Research: Atmospheres, 123, 10,410-464,476, https://doi.org/10.1029/2018JD028381, 2018.

Kanji, Z. A., Ladino, L. A., Wex, H., Boose, Y., Burkert-Kohn, M., Cziczo, D. J., and Krämer, M.: Overview of ice nucleating particles, Meteorological Monographs, 58, 1.1-1.33, https://doi.org/10.1175/AMSMONOGRAPHS-D-16-0006.1, 2017.

Kärcher, B., Hendricks, J., and Lohmann, U.: Physically based parameterization of cirrus cloud formation for use in global atmospheric models, Journal of Geophysical Research: Atmospheres, 111, https://doi.org/10.1029/2005JD006219, 2006.

Kay, J. E., L'Ecuyer, T., Pendergrass, A., Chepfer, H., Guzman, R., and Yettella, V.: Scale-aware and definition-aware evaluation of modeled near-surface precipitation frequency using CloudSat observations, Journal of Geophysical Research: Atmospheres, 123, 4294-4309, https://doi.org/10.1002/2017JD028213, 2018.

Keil, C., Baur, F., Bachmann, K., Rasp, S., Schneider, L., and Barthlott, C.: Relative contribution of soil moisture, boundary-layer and microphysical perturbations on convective predictability in different weather regimes, Quarterly Journal of the Royal Meteorological Society, 145, 3102-3115, https://doi.org/10.1002/qj.3607, 2019.

Korolev, A. and Isaac, G. A.: Relative humidity in liquid, mixed-phase, and ice clouds, Journal of the Atmospheric Sciences, 63, 2865-2880, https://doi.org/10.1175/JAS3784.1, 2006.

Korolev, A.: Limitations of the Wegener–Bergeron–Findeisen mechanism in the evolution of mixed-phase clouds, Journal of the Atmospheric Sciences, 64, 3372-3375, http://dx.doi.org/10.1175/JAS4035.1, 2007.

Korolev, A., McFarquhar, G., Field, P. R., Franklin, C., Lawson, P., Wang, Z., Williams, E., Abel, S. J., Axisa, D., Borrmann, S., Crosier, J., Fugal, J., Krämer, M., Lohmann, U., Schlenczek, O., Schnaiter, M., and Wendisch, M.: Mixed-phase clouds: Progress and challenges, Meteorological Monographs, 58, 5.1-5.50, https://doi.org/10.1175/AMSMONOGRAPHS-D-17-0001.1, 2017.

Korolev, A. V., Isaac, G. A., Cober, S. G., Strapp, J. W., and Hallett, J.: Microphysical characterization of mixed-phase clouds, Quarterly Journal of the Royal Meteorological Society, 129, 39-65, https://doi.org/10.1256/qj.01.204, 2003.

Li, R. and Min, Q. L.: Impacts of mineral dust on the vertical structure of precipitation, Journal of Geophysical Research: Atmospheres, 115, https://doi.org/10.1029/2009JD011925, 2010.

Li, X., Tao, W.-K., Masunaga, H., Masunaga, Gu, G., and Zeng, X.: Aerosol effects on cumulus congestus population over the tropical acific: A cloud-resolving

823 modeling study, Journal of the Meteorological Society of Japan, 91, 817-833,
824 10.2151/jmsj.2013-607, 2013.

825 Lohmann, U. and Hoose, C.: Sensitivity studies of different aerosol indirect effects in
826 mixed-phase clouds, Atmos. Chem. Phys., 9, 8917-8934,
827 https://doi.org/10.5194/acp-9-8917-2009, 2009.

828 Matus, A. V. and L'Ecuyer, T. S.: The role of cloud phase in Earth's radiation budget,
829 Journal of Geophysical Research: Atmospheres, 122, 2559-2578,
830 https://doi.org/10.1002/2016JD025951, 2017.

831 McCoy, D. T., Tan, I., Hartmann, D. L., Zelinka, M. D., and Storelvmo, T.: On the
832 relationships among cloud cover, mixed-phase partitioning, and planetary
833 albedo in GCMs, Journal of Advances in Modeling Earth Systems, 8, 650-668,
834 https://doi.org/10.1002/2015MS000589, 2016.

835 Mecikalski, J. R., Jewett, C. P., Apke, J. M., and Carey, L. D.: Analysis of Cumulus
836 Cloud Updrafts as Observed with 1-Min Resolution Super Rapid Scan GOES
837 Imagery, Monthly Weather Review, 144, 811-830,
838 https://doi.org/10.1175/MWR-D-14-00399.1, 2016.

839 Mellado, J. P.: Cloud-top entrainment in stratocumulus clouds, Annual Review of
840 Fluid Mechanics, 49, 145-169, 10.1146/annurev-fluid-010816-060231, 2017.

841 Menzel, W. P., Smith, W. L., and Stewart, T. R.: Improved cloud motion wind vector
842 and altitude assignment using VAS, Journal of Applied Meteorology and
843 Climatology, 22, 377-384, https://doi.org/10.1175/1520-
844 0450(1983)022<0377:ICMWVA>2.0.CO;2, 1983.

845 Miltenberger, A. K. and Field, P. R.: Sensitivity of mixed-phase moderately deep
846 convective clouds to parameterizations of ice formation – an ensemble
847 perspective, Atmos. Chem. Phys., 21, 3627-3642,
848 http://dx.doi.org/10.5194/acp-21-3627-2021, 2021.

849 Min, Q. L., Li, R., Lin, B., Joseph, E., Wang, S., Hu, Y., Morris, V., and Chang, F.:
850 Evidence of mineral dust altering cloud microphysics and precipitation,
851 Atmospheric Chemistry and Physics, 9, 3223-3231,
852 https://doi.org/10.5194/acp-9-3223-2009, 2009.

853 Nakajima, T. and King, M. D.: Determination of the optical thickness and effective
854 particle radius of clouds from reflected solar radiation measurements. Part I:
855 Theory, Journal of Atmospheric Sciences, 47, 1878-1893,
856 https://doi.org/10.1175/1520-0469(1990)047<1878:DOTOTA>2.0.CO;2, 1990.

857 Noh, Y.-J., Seaman, C. J., Vonder Haar, T. H., and Liu, G.: In situ aircraft
858 measurements of the vertical distribution of liquid and ice water content in
859 midlatitude mixed-phase clouds, Journal of Applied Meteorology and
860 Climatology, 52, 269-279, https://doi.org/10.1175/JAMC-D-11-0202.1, 2013.

861 Pavolonis, M. J., Heidinger, A. K., and Uttal, T.: Daytime global cloud typing from
862 AVHRR and VIIRS: Algorithm description, validation, and comparisons,
863 Journal of Applied Meteorology, 44, 804-826,
864 https://doi.org/10.1175/JAM2236.1, 2005.

865 Pinto, J. O.: Autumnal mixed-phase cloudy boundary layers in the Arctic, Journal of
866 the Atmospheric Sciences, 55, 2016-2038, https://doi.org/10.1175/1520-
867 0469(1998)055<2016:AMPCBL>2.0.CO;2, 1998.

868 Pscheidt, I., Senf, F., Heinze, R., Deneke, H., Trömel, S., and Hohenegger, C.: How
869 organized is deep convection over Germany?, Quarterly Journal of the Royal
870 Meteorological Society, 145, 2366-2384, http://dx.doi.org/10.1002/qj.3552,
871 2019.

Roebeling, R. A., Feijt, A. J., and Stammes, P.: Cloud property retrievals for climate monitoring: Implications of differences between Spinning Enhanced Visible and Infrared Imager (SEVIRI) on METEOSAT-8 and Advanced Very High Resolution Radiometer (AVHRR) on NOAA-17, Journal of Geophysical Research: Atmospheres, 111, https://doi.org/10.1029/2005JD006990, 2006.

Rosenfeld, D. and Woodley, W. L.: Deep convective clouds with sustained supercooled liquid water down to -37.5 °C, Nature, 405, 440-442, https://doi.org/10.1038/35013030, 2000.

Rosenfeld, D., Yu, X., Liu, G., Xu, X., Zhu, Y., Yue, Z., Dai, J., Dong, Z., Dong, Y., and Peng, Y.: Glaciation temperatures of convective clouds ingesting desert dust, air pollution and smoke from forest fires, Geophysical Research Letters, 38, https://doi.org/10.1029/2011GL049423, 2011.

Rybka, H., Burkhardt, U., Köhler, M., Arka, I., Bugliaro, L., Görsdorf, U., Horváth, Á., Meyer, C. I., Reichardt, J., Seifert, A., and Strandgren, J.: The behavior of high-CAPE (convective available potential energy) summer convection in large-domain large-eddy simulations with ICON, Atmos. Chem. Phys., 21, 4285-4318, http://dx.doi.org/10.5194/acp-21-4285-2021, 2021.

Saunders, R., Hocking, J., Turner, E., Rayer, P., Rundle, D., Brunel, P., Vidot, J., Roquet, P., Matricardi, M., Geer, A., Bormann, N., and Lupu, C.: An update on the RTTOV fast radiative transfer model (currently at version 12), Geosci. Model Dev., 11, 2717-2737, http://dx.doi.org/10.5194/gmd-11-2717-2018, 2018.

Schmetz, J., Holmlund, K., Hoffman, J., Strauss, B., Mason, B., Gaertner, V., Koch, A., and Van De Berg, L.: Operational cloud-motion winds from meteosat infrared images, Journal of Applied Meteorology and Climatology, 32, 1206-1225, https://doi.org/10.1175/1520-0450(1993)032<1206:OCMWFM>2.0.CO;2, 1993.

Schmetz, J., Pili, P., Tjemkes, S., Just, D., Kerkmann, J., Rota, S., and Ratier, A.: An introduction to meteosat second generation (MSG), Bulletin of the American Meteorological Society, 83, 977-992, http://dx.doi.org/10.1175/1520-0477(2002)083<0977:AITMSG>2.3.CO;2, 2002.

Seifert, A. and Beheng, K. D.: A two-moment cloud microphysics parameterization for mixed-phase clouds. Part 1: Model description, Meteorology and Atmospheric Physics, 92, 45-66, http://dx.doi.org/10.1007/s00703-005-0112-4, 2006.

Senf, F., Voigt, A., Clerbaux, N., Hünerbein, A., and Deneke, H.: Increasing resolution and resolving convection improve the simulation of cloud-radiative effects over the North Atlantic, Journal of Geophysical Research: Atmospheres, 125, e2020JD032667, https://doi.org/10.1029/2020JD032667, 2020.

Sheffield, A. M., Saleeby, S. M., and van den Heever, S. C.: Aerosol-induced mechanisms for cumulus congestus growth, Journal of Geophysical Research: Atmospheres, 120, 8941-8952, https://doi.org/10.1002/2015JD023743, 2015.

Sotiropoulou, G., Vignon, É., Young, G., Morrison, H., O'Shea, S. J., Lachlan-Cope, T., Berne, A., and Nenes, A.: Secondary ice production in summer clouds over the Antarctic coast: an underappreciated process in atmospheric models, Atmos. Chem. Phys., 21, 755-771, https://doi.org/10.5194/acp-21-755-2021, 2021.

Stengel, M., Kniffka, A., Meirink, J. F., Lockhoff, M., Tan, J., and Hollmann, R.: CLAAS: the CM SAF cloud property data set using SEVIRI, Atmos. Chem. Phys., 14, 4297-4311, http://dx.doi.org/10.5194/acp-14-4297-2014, 2014.

Stephens, G. L.: Radiation profiles in extended water clouds. II: Parameterization schemes, Journal of Atmospheric Sciences, 35, 2123-2132, https://doi.org/10.1175/1520-0469(1978)035<2123:RPIEWC>2.0.CO;2, 1978.

Stith, J. L., Haggerty, J. A., Heymsfield, A., and Grainger, C. A.: Microphysical characteristics of tropical updrafts in clean conditions, Journal of Applied Meteorology, 43, 779-794, https://doi.org/10.1175/2104.1, 2004.

Sullivan, S. C., Barthlott, C., Crosier, J., Zhukov, I., Nenes, A., and Hoose, C.: The effect of secondary ice production parameterization on the simulation of a cold frontal rainband, Atmos. Chem. Phys., 18, 16461-16480, https://doi.org/10.5194/acp-18-16461-2018, 2018.

Takeishi, A. and Storelvmo, T.: A study of enhanced heterogeneous ice nucleation in simulated deep convective clouds observed during DC3, Journal of Geophysical Research: Atmospheres, 123, 13,396-313,420, https://doi.org/10.1029/2018JD028889, 2018.

Taylor, J. W., Choularton, T. W., Blyth, A. M., Liu, Z., Bower, K. N., Crosier, J., Gallagher, M. W., Williams, P. I., Dorsey, J. R., Flynn, M. J., Bennett, L. J., Huang, Y., French, J., Korolev, A., and Brown, P. R. A.: Observations of cloud microphysics and ice formation during COPE, Atmos. Chem. Phys., 16, 799-826, https://doi.org/10.5194/acp-16-799-2016, 2016.

Thomas, J., Barrett, A., and Hoose, C.: Temperature and cloud condensation nuclei (CCN) sensitivity of orographic precipitation enhanced by a mixed-phase seeder–feeder mechanism: a case study for the 2015 Cumbria flood, Atmos. Chem. Phys., 23, 1987-2002, 10.5194/acp-23-1987-2023, 2023.

Twohy, C. H.: Measurements of Saharan dust in convective clouds over the tropical eastern Atlantic ocean, Journal of the Atmospheric Sciences, 72, 75-81, https://doi.org/10.1175/JAS-D-14-0133.1, 2015.

van den Heever, S. C., Carrió, G. G., Cotton, W. R., DeMott, P. J., and Prenni, A. J.: Impacts of nucleating aerosol on Florida storms. Part I: Mesoscale simulations, Journal of the Atmospheric Sciences, 63, 1752-1775, https://doi.org/10.1175/JAS3713.1, 2006.

Vignon, É., Alexander, S. P., DeMott, P. J., Sotiropoulou, G., Gerber, F., Hill, T. C. J., Marchand, R., Nenes, A., and Berne, A.: Challenging and improving the simulation of mid-level mixed-phase clouds over the high-latitude southern ocean, Journal of Geophysical Research: Atmospheres, 126, e2020JD033490, https://doi.org/10.1029/2020JD033490, 2021.

Wan, H., Giorgetta, M. A., Zängl, G., Restelli, M., Majewski, D., Bonaventura, L., Fröhlich, K., Reinert, D., Rípodas, P., Kornblueh, L., and Förstner, J.: The ICON-1.2 hydrostatic atmospheric dynamical core on triangular grids – Part 1: Formulation and performance of the baseline version, Geosci. Model Dev., 6, 735-763, http://dx.doi.org/10.5194/gmd-6-735-2013, 2013.

Zängl, G., Reinert, D., Rípodas, P., and Baldauf, M.: The ICON (ICOsahedral Non-hydrostatic) modelling framework of DWD and MPI-M: Description of the non-hydrostatic dynamical core, Quarterly Journal of the Royal Meteorological Society, 141, 563-579, http://dx.doi.org/10.1002/qj.2378, 2015.

Zhao, B., Wang, Y., Gu, Y., Liou, K.-N., Jiang, J. H., Fan, J., Liu, X., Huang, L., and Yung, Y. L.: Ice nucleation by aerosols from anthropogenic pollution, Nature Geoscience, 12, 602-607, https://doi.org/10.1038/s41561-019-0389-4, 2019.

971   Zhao, X., Liu, X., Burrows, S. M., and Shi, Y.: Effects of marine organic aerosols as
972   sources of immersion-mode ice-nucleating particles on high-latitude mixed-
973   phase clouds, Atmos. Chem. Phys., 21, 2305-2327,
974   https://doi.org/10.5194/acp-21-2305-2021, 2021.
975

976 **Tables:**

977

978 Table 1: Setups of simulations performed in this study.

Num	Experiment	Description
1	$A\times10^0$ (CTRL)	Without any perturbations, the CTRL run, used as a reference.
2	$A\times10^{-2}$	INP concentrations for both immersion and deposition mode are scaled by multiplying parameter A in Equation (1) by 10^{-2}.
3	$A\times10^{-1}$	Same as num. 2, but multiplying by 10^{-1}.
4	$A\times10^1$	Same as num. 2, but multiplying by 10^1.
5	$A\times10^2$	Same as num. 2, but multiplying by 10^2.
6	$A\times10^3$	Same as num. 2, but multiplying by 10^3.
7	$A\times10^0$_NSIP	INP concentration as in CTRL. The secondary ice production (rime-splintering process) is switched off.
8	DEC05	Initial and lateral temperature decreases from 3 to 12 km with a maximum increment of 5 K. No perturbations in INPs ($A\times10^0$).
9	DEC03	Same as num. 8, but with a maximum increment of 3 K.
10	INC03	Initial and lateral temperature increases from 3 to 12 km with a maximum increment of 3 K. No perturbations in INPs ($A\times10^0$).
11	INC05	Same as num. 10, but with a maximum increment of 5 K.

979

980

981

982

983 **Figures:**

984

985
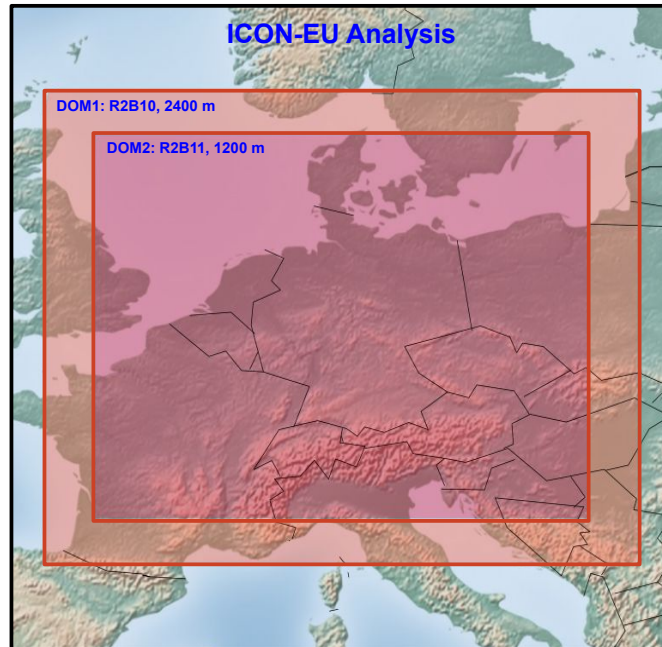
986

987 Figure 1: The simulation domains.

988

989

990
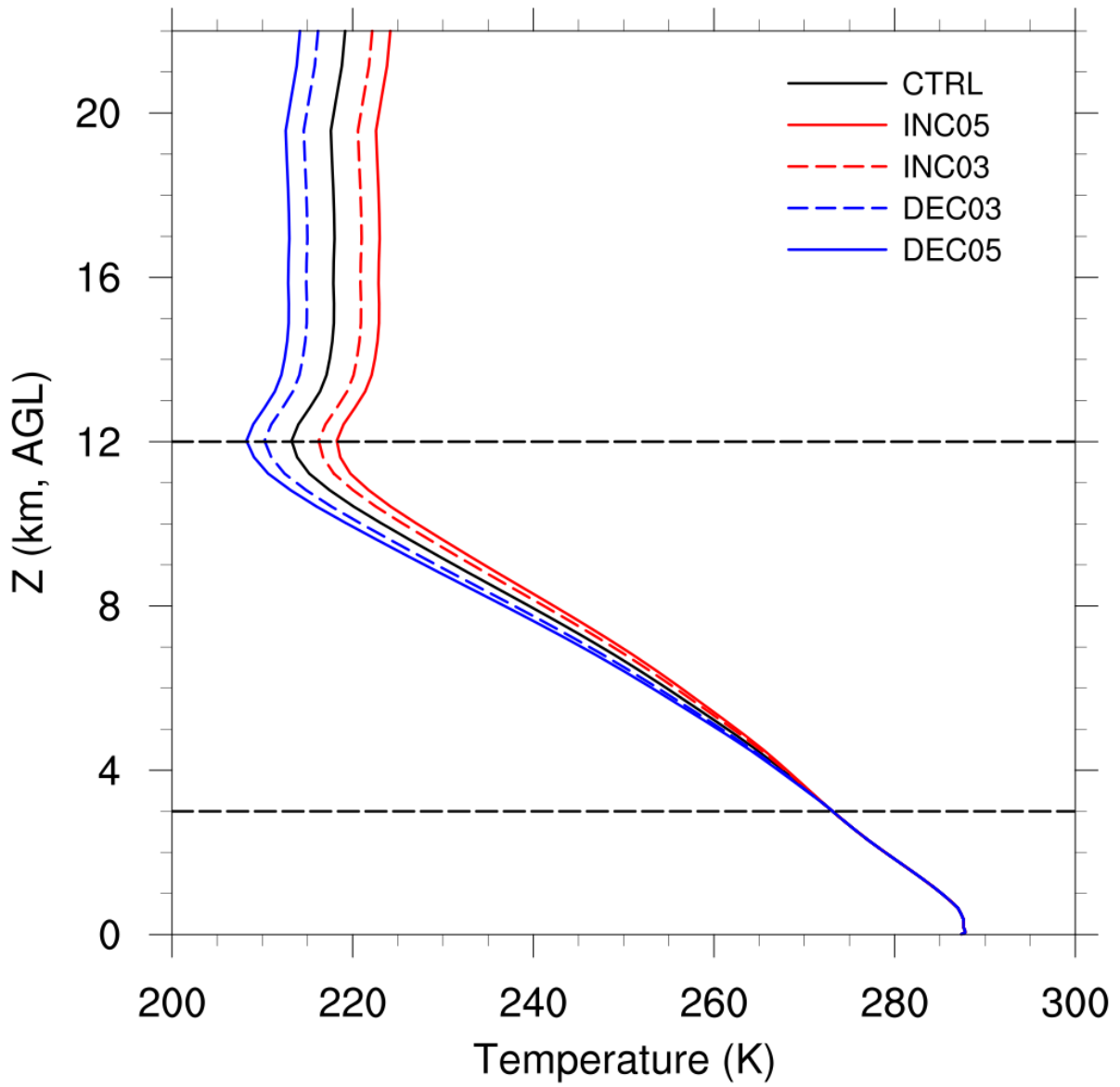
Figure 2: Domain averaged initial temperature profiles. The same modification was applied to the lateral boundary conditions.

993
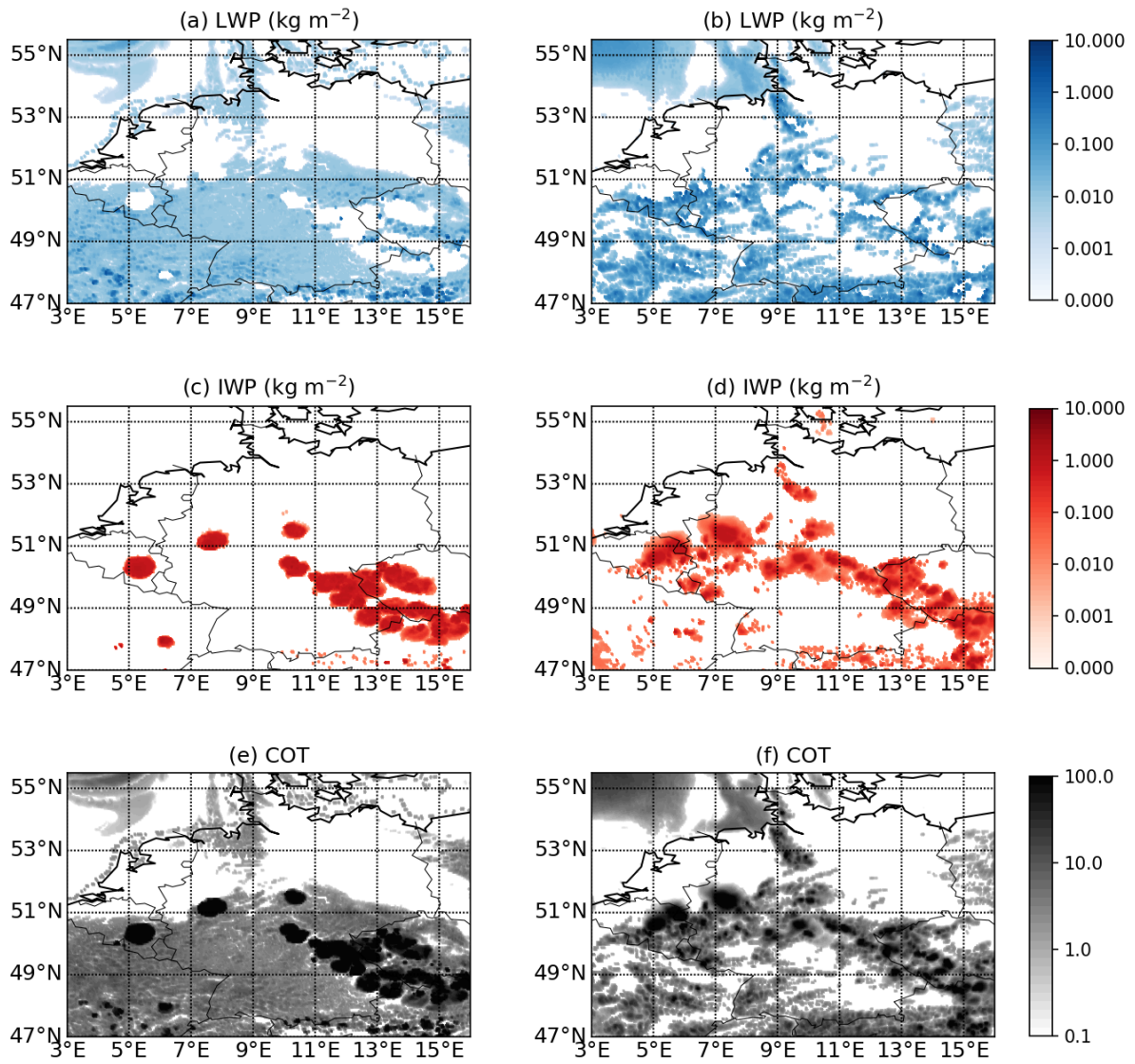
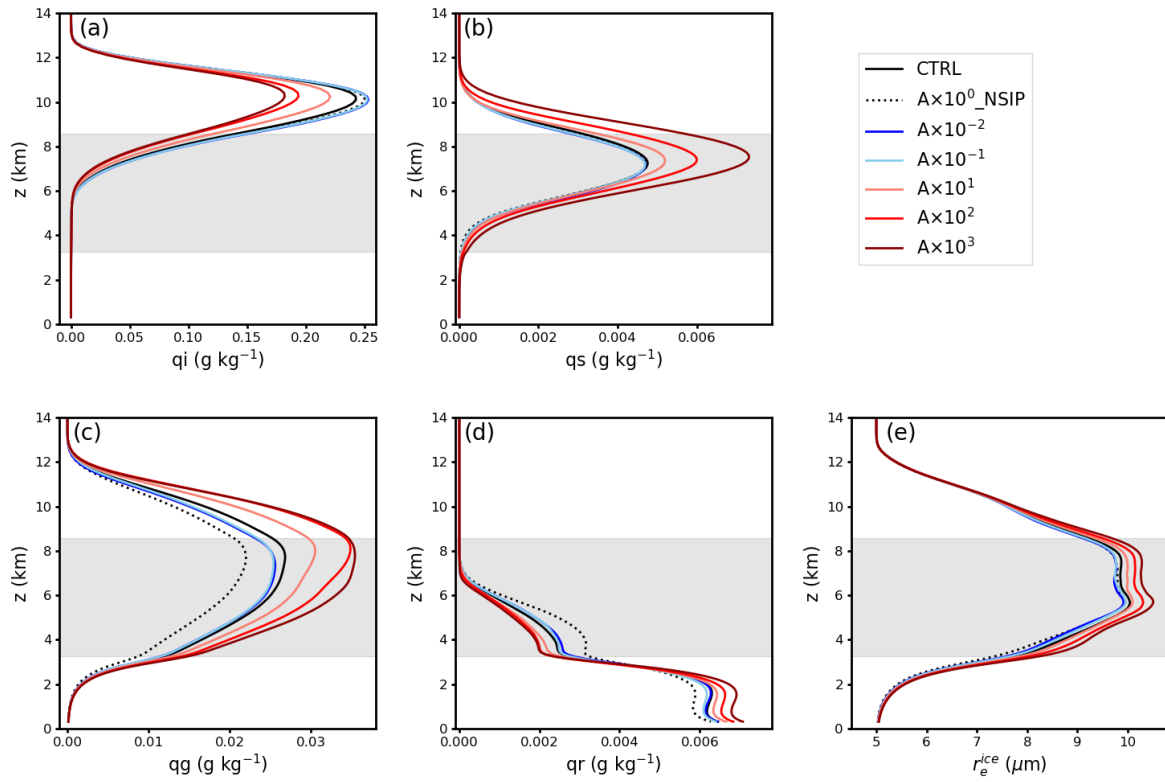Figure 3: Spatial distributions of retrieved cloud liquid water path (LWP), ice water path (IWP), and cloud optical thickness (COT) at 13:00 UTC. The left panel is for the CTRL case (a, c, e) and the right panel is for the CLAAS-2 product (b, d, f).

999
1000 Figure 4: Spatial- and time-averaged (9:00~19:00) profiles of cloud mass mixing
1001 ratios of (a) ice crystals, (b) snow, (c) graupel, (d) rainwater, and (e) ice crystal
1002 effective radius. Mass mixing ratio unit is g kg^{-1} and the unit of ice crystal effective
1003 radius is μm. Shaded area indicates the spatial- and time-averaged mixed-phase
1004 region.

1005
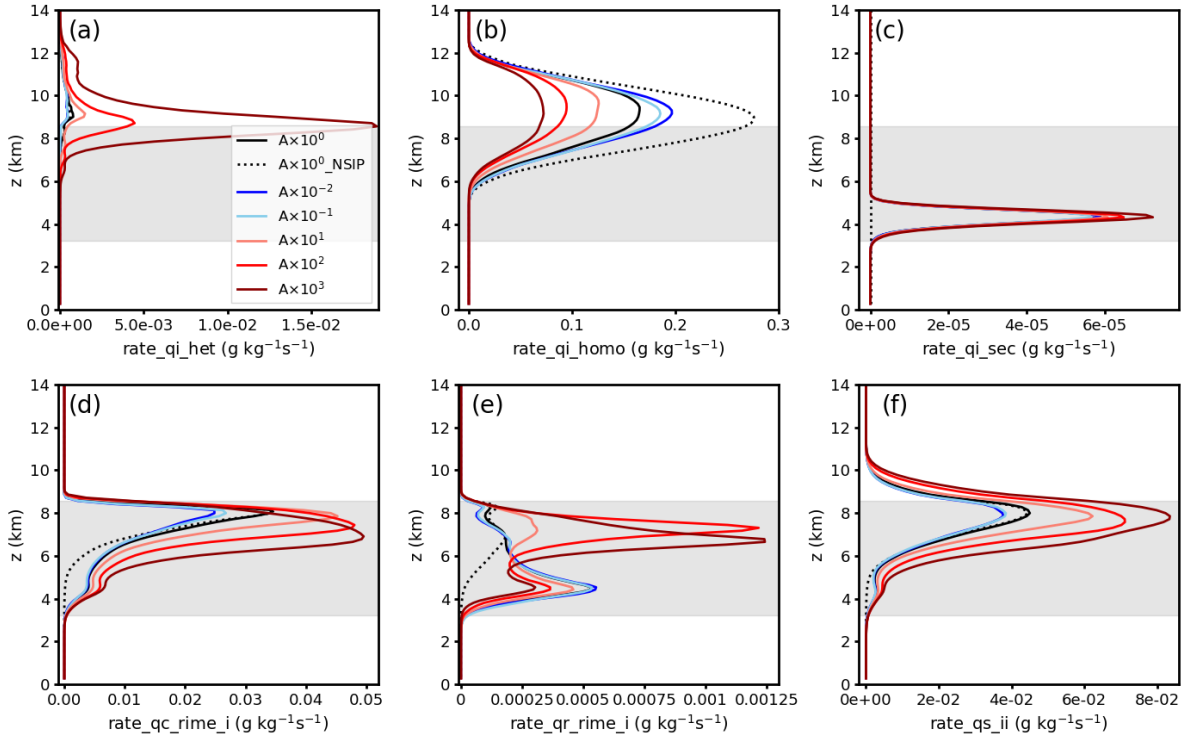
Figure 5: Spatial- and time-averaged (9:00~19:00) profiles of process rates of (a) heterogeneous freezing (immersion and deposition nucleation), (b) homogeneous freezing, (c) secondary-ice production (rime-splintering), (d) cloud droplets rimed with ice crystals, (e) rain droplets rimed with ice crystals, (f) collection between ice and ice. Unit is g kg-1 s-1. The average mixed-phase layer (0~-38 °C) is roughly in between 3.2 and 8.6 km. Shaded area indicates the spatial- and time-averaged mixed-phase region. Unit is g kg^{-1}s^{-1}.
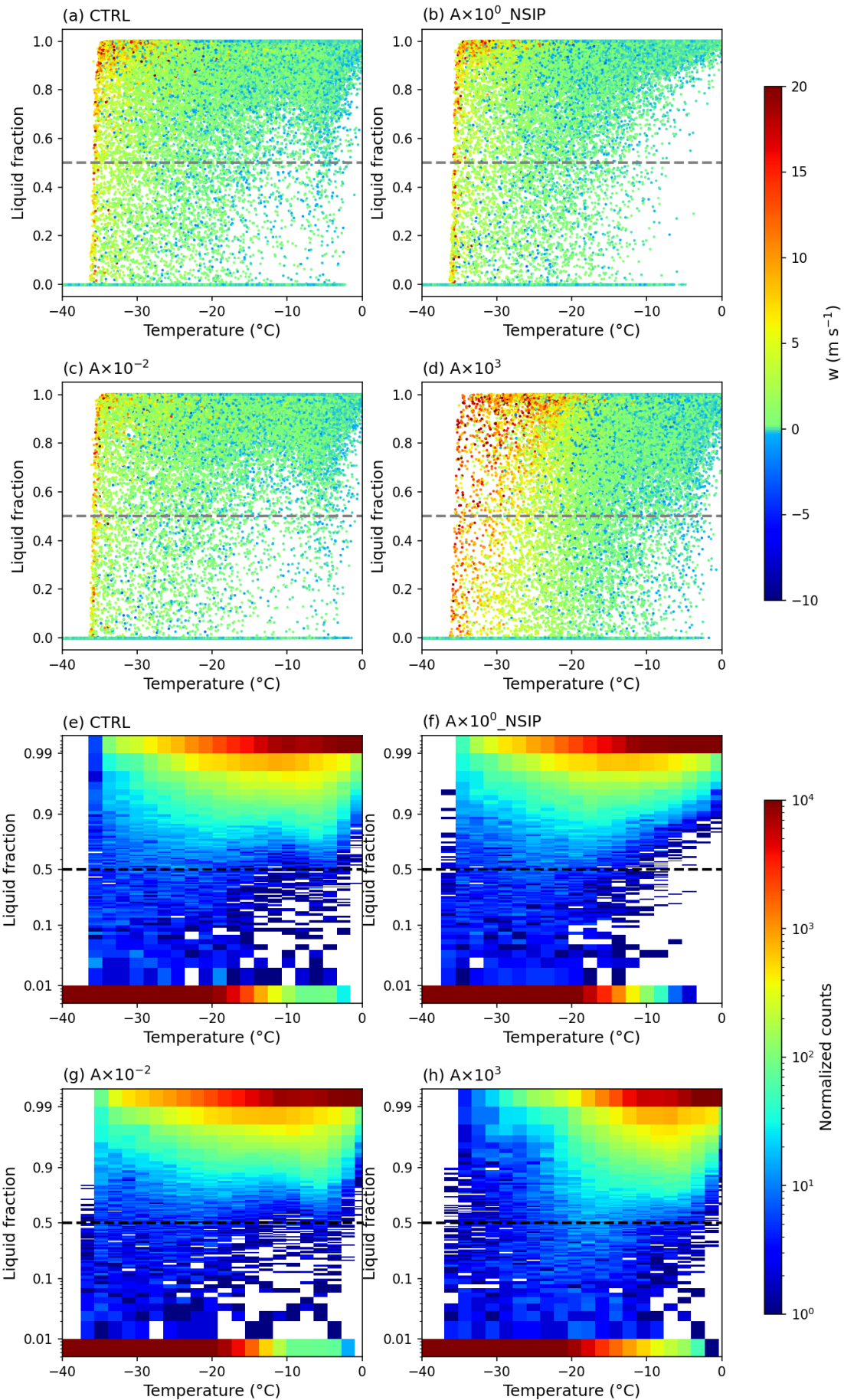
1016   Figure 6: In-cloud supercooled liquid mass fraction distribution as a function of

1017   temperature (binned by 1°C) between 9:00 and 19:00 (a-d) for the 4 cases ($A \times 10^0$,

1018 $A \times 10^0$_NSIP, $A \times 10^{-2}$, $A \times 10^3$), the colour of points indicates the vertical wind velocity

1019   (unit, m s^{-1}). 2-D histogram of in-cloud liquid mass fraction versus temperature (e-f).
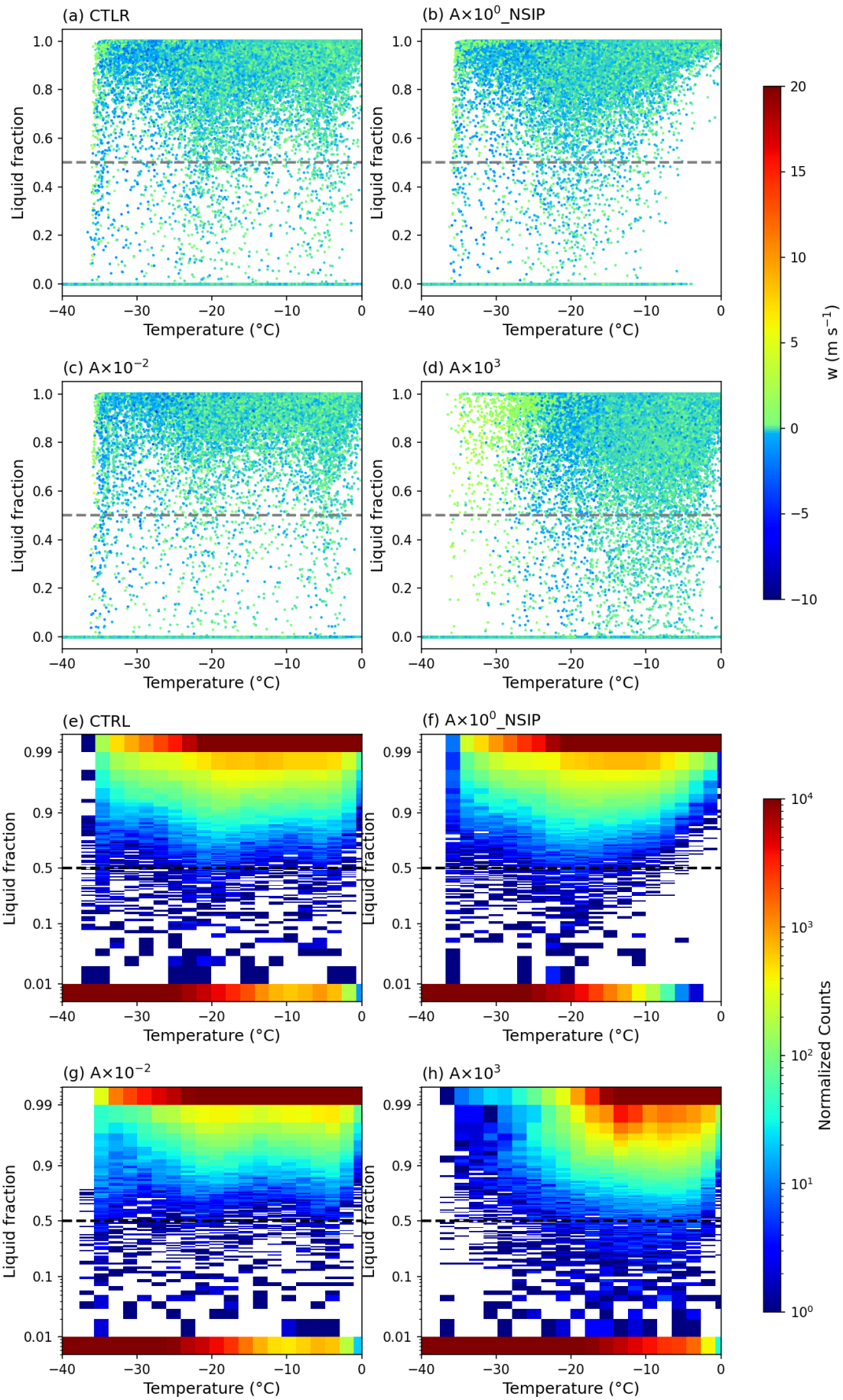
1021 Figure 7: Cloud-top supercooled liquid mass fraction distribution as a function of
1022 temperature (binned by 1°C) between 9:00 and 19:00 (a-d) for the 4 cases ($A\times10^0$,
1023 $A\times10^0$_NSIP, $A\times10^{-2}$, $A\times10^3$), the colour of points indicates the vertical wind velocity
1024 (unit, m s^{-1}). 2-D histogram of cloud-top liquid mass fraction versus temperature (e-f).
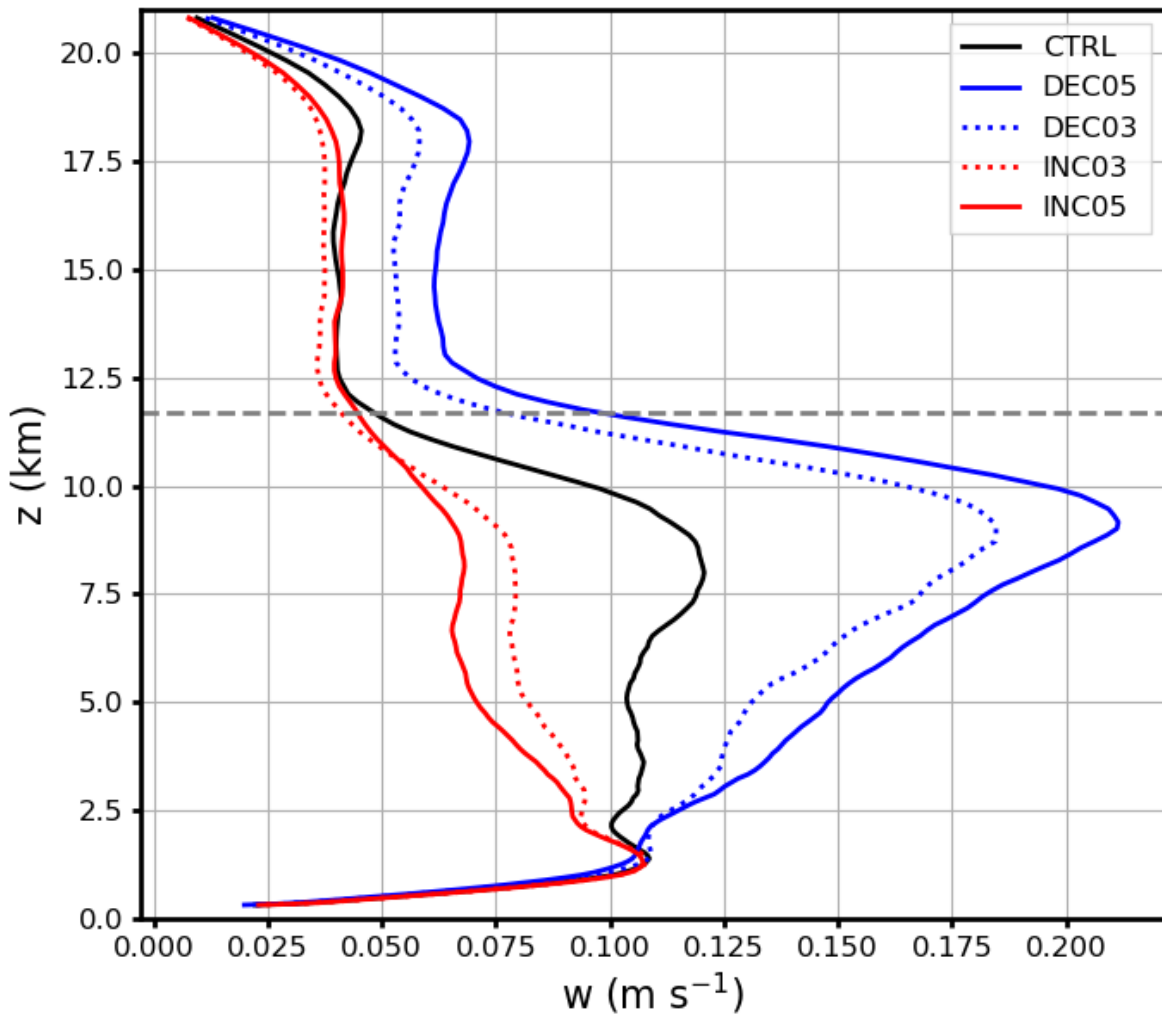
1025
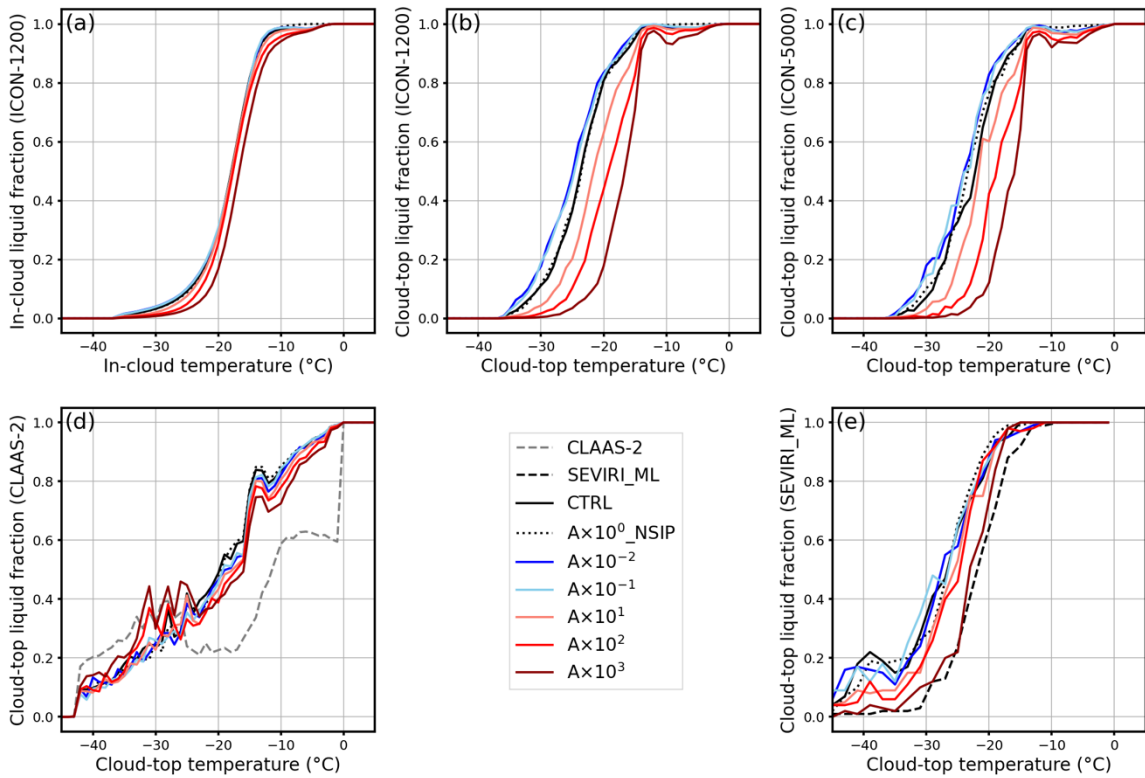
1026

1027 Figure 8: Liquid cloud pixel fraction as a function of temperature from 9:00 to 19:00
1028 UTC for the INP sensitivity experiments, (a) in-cloud fraction calculated from
1029 simulations on ICON native grid (~1200 m), (b) cloud-top fraction calculated from
1030 simulations on ICON native grid (~1200 m), (c) cloud-top fraction calculated from
1031 simulations on SEVIRI's grid (~5000 m), (d) cloud-top fraction calculated by remote-
1032 sensing retrieval algorithms to produce CLAAS-2 dataset, and (e) cloud-top fraction
1033 calculated by remote-sensing retrieval software suite SEVIRI_ML. The temperature
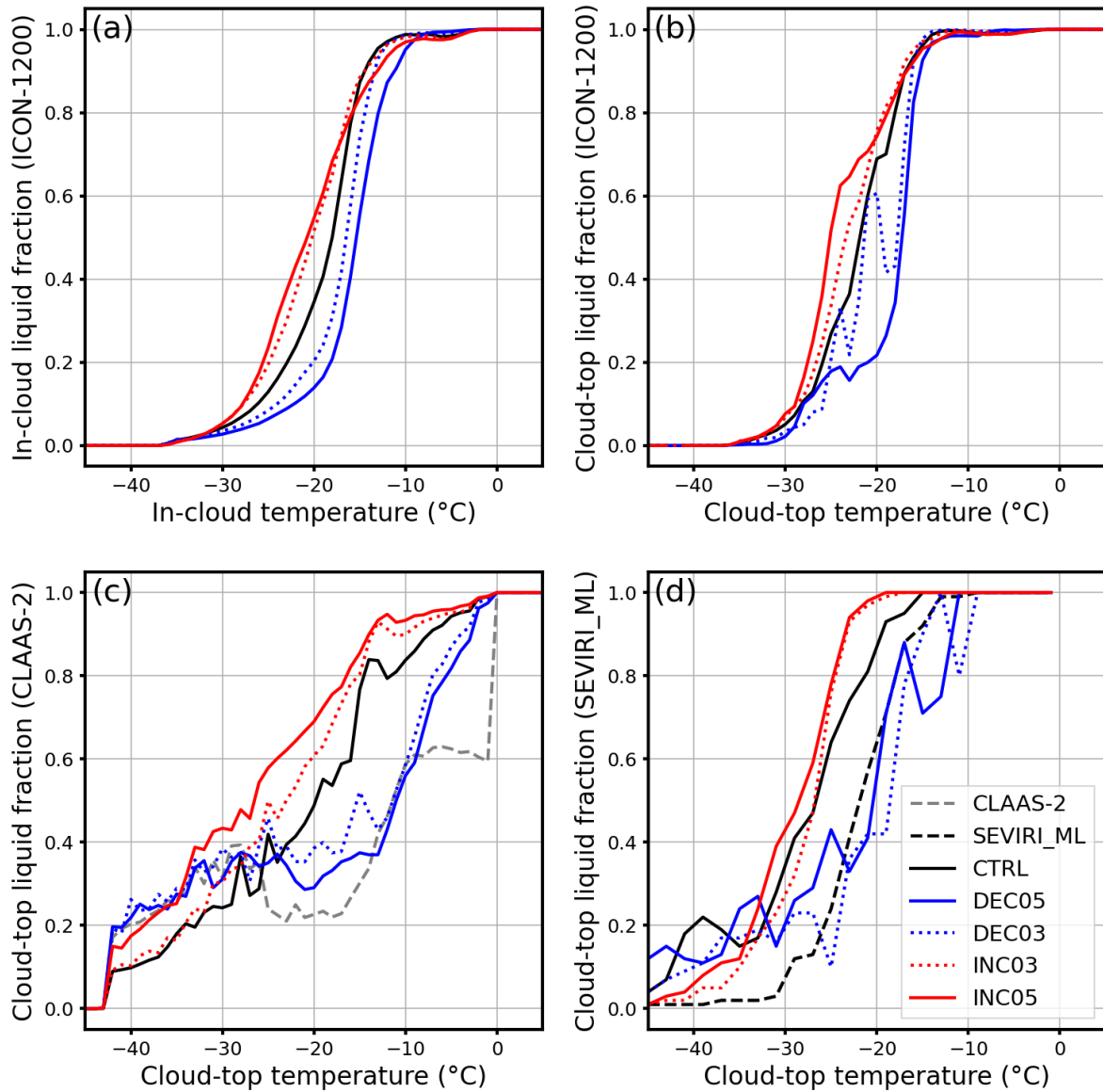1034 is binned by 1°C in (a), (b), (c), and (d), and by 2°C in (e).

1035

1036

1037
1038 Figure 9: Spatial- and time-averaged (9:00~19:00) profiles of vertical velocities (w
1039 values ≤ 0 m s^{-1} are excluded). The dashed grey line indicates the clout top height
1040 which is about 11.7 km.

1041

1044 Figure 10: Liquid cloud pixel fraction as a function of temperature from 9:00 to 19:00
1045 for the thermodynamic sensitivity experiments, (a) in-cloud fraction calculated
1046 directly from simulations, (b) cloud-top fraction calculated from directly simulations,
1047 (c) cloud-top fraction calculated by remote-sensing retrieval algorithms to produce
1048 CLAAS-2 dataset, and (d) cloud-top fraction calculated by remote-sensing retrieval
1049 software suite SEVIRI_ML. The temperature is binned by 1°C in (a), (b), and (c), and
1050 by 2°C in (d).

1051

1052
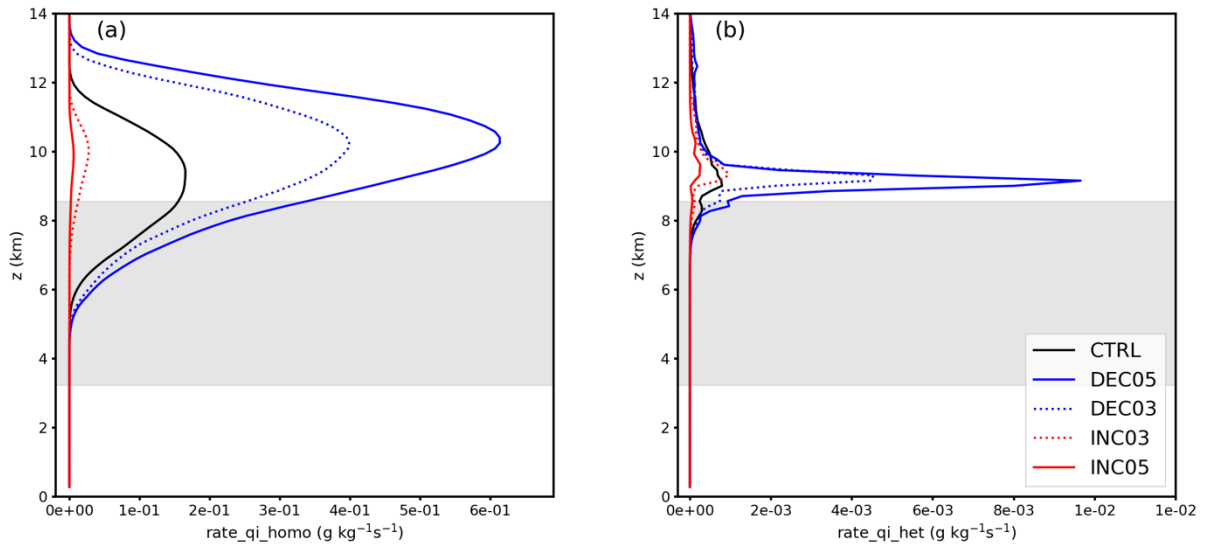
1053

1054 Figure 11: Spatial- and time-averaged (9:00~19:00) profiles of process rates of (a)
1055 homogeneous freezing, (b) heterogeneous freezing (immersion and deposition
1056 nucleation) for cases with perturbed initial thermodynamic states. Shaded area
1057 indicates the spatial and time-averaged mixed-phase region. Unit is g kg^{-1} s^{-1}.

1058